Mechanical and Cooling Design Studies for an Integrated Stave Concept for Silicon Strip Detectors for the Super LHC

M. Cepeda [a]**, S. Dardin** [a]**, M. Gilchriese** [a] *****, **C. Haber** [a]**, W. K. Miller** [b]**, W. O. Miller** [b]
and R. Post [a]

[a] *Lawrence Berkeley National Laboratory,*
  1 Cyclotron Rd, Berkeley CA 94720, USA

[b] *Innovative Technology International,*
  Albuquerque, NM 87111, USA
  E-mail: MGGilchriese@lbl.gov

ABSTRACT: Design studies for the mechanical and thermal performance of an integrated stave concept for large-area silicon-strip detector support and cooling are described. The fabrication and test of small-scale prototypes are also presented. Finite-element and other calculations have been completed to develop the design concept and to compare with the measurements on prototypes.

June 18, 2008

***** Corresponding author.

Contents

1. Introduction and Overview of Concept

A possible layout for ATLAS inner detector for the Super Large Hadron Collider (SLHC) has been described.[1] A cross-section of this layout is shown in Figure 1.
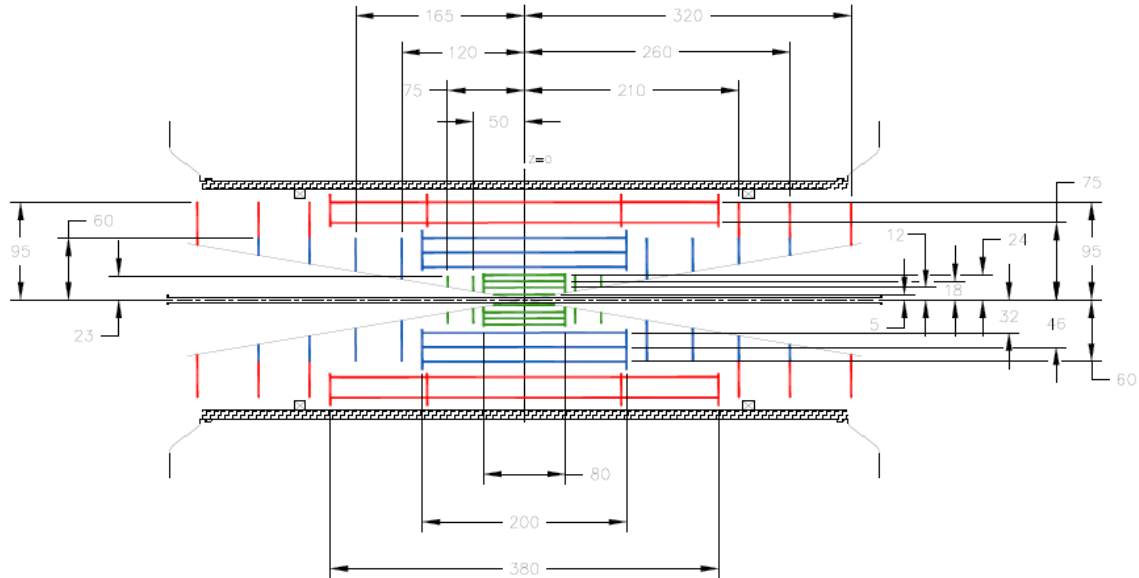

Figure 1 Possible layout of inner detector for the SLHC. Short-strip (SS) layers are indicated in blue in this figure and long-strip (LS) layers are indicated in red. Pixel layers are indicated in green.

The silicon strip detectors are arrayed in short-strip (SS) regions and long-strip (LS) regions, as shown schematically in Figure 1. The barrel short-strip layers are about 2 m long and the barrel long-strip layers are about 4 m long in this layout (alternative layouts with equal-length barrels are also under investigation).

The concept of an integrated stave for the barrel region of the tracker is illustrated in Figure 2.[2] The baseline integrated stave concept consists of the following elements:

- a mechanical support with integrated cooling – the mechanical core of the concept;
- a bus cable(copper-aluminum-kapton flex-circuit to distribute electrical signals, power and high-voltage) laminated to the mechanical core (one on each side of the core)
- single-sided, silicon detector modules (hybrid with readout electronics and silicon sensor) glued to the bus cables; and
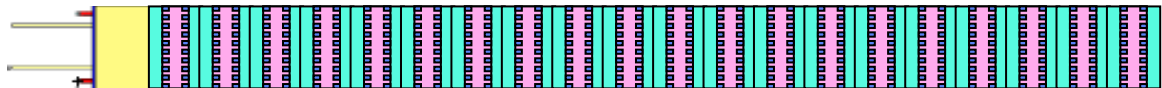- an end-of-stave card for stave-level readout and control.

Figure 2 Concept of an integrated stave with short-strip silicon detectors. The end-of-stave card would be located in the region at the left-end of the stave (yellow region) in this conceptual drawing. Modules are mounted on both sides of the stave.

A cross-section of the mechanical core is shown in Figure 3. The basic components of the mechanical core are the following:

- facings (nominally carbon-fiber) on both sides of the stave to which the bus cable is laminated.
- core material (honeycomb or carbon foam or both) between the facings to provide stiffness to the overall structure. The thickness of the core material depends on the size of the coolant pipe, which in-turn depends on the type of coolant.
- a cooling pipe assembly that may consist of just a pipe bonded (with a thermal adhesive) to the facings or a round-pipe with a surrounding, thermally-conducting carbon foam that is bonded to the facings as well as the tube.
- end structures (not shown in Figure 2 or Figure 3) for possible strain relief of the cooling tubes or cables/fibers from the end-of-stave card and mounting points (on the side, also not shown) that interface with an external support structure.
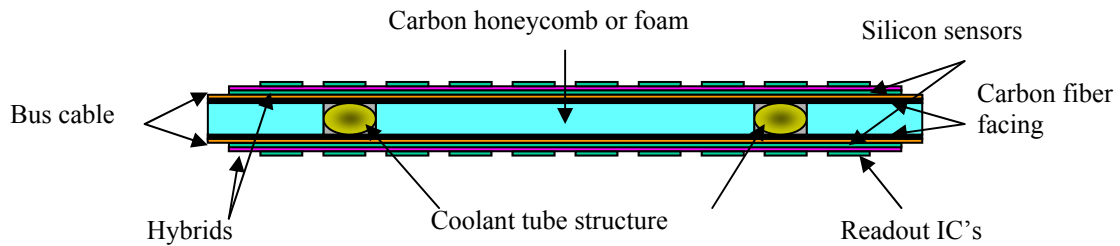

Figure 3 Cross-section of the mechanical/cooling core of the integrated stave concept.

The baseline design is based on using silicon sensors that are about 10 cm x 10 cm in all regions, internally segmented to provide short-strips (about 2.5 cm long) or long-strips (about 10 cm long). The length of a stave depends on the final layout. Our baseline assumption is that the length for the short-strip (long-strip) region is about 1 m (2 m). The minimum thickness of the stave mechanical core (not including bus cable or modules) is approximately 3.5 mm for CO_2 coolant and about 6.5 mm for C_3F_8 coolant (these values for thickness are derived in later sections). Apart from the aluminum cooling tube and adhesives, the baseline design for the mechanical core utilizes only carbon-based materials.*

2. Prototype Fabrication and Tests

A number of stave prototypes were fabricated and a summary is given in Table 1. We note that the width of the prototypes was set in 2006 well before a decision was made to use 10 cm x 10 cm detectors for the SLHC upgrade and therefore the width of the prototype staves is smaller, about 7.2 cm, as shown in Figure 4.

---

* Mounting points (not yet designed) may include metal parts eg. screws or bolts.
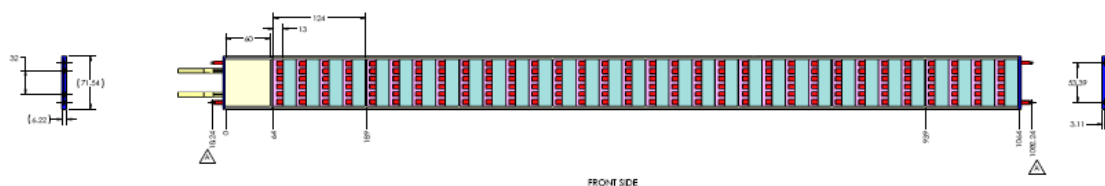
Figure 4 Dimensions of the full-length, prototype stave.

The prototypes were fabricated to address the following goals: (a) to gain experience in the fabrication techniques for the design; (b) to fabricate three, short prototypes with different tube configurations to explore a range of options applicable to different potential coolants (C_3F_8, potential mixtures of other fluorocarbons with C_3F_8 and CO_2) and to measure their thermal performance; and (c) to make a full-length (1m) prototype to be used to mount prototype modules. In addition, the facing thickness (stiffness) was also varied. The thermal performance of three prototypes (numbers 2, 4 and 5 in Table 1) was measured. Profile and deflection measurements were made on the full-length prototype and prototype #2.

Prototype Number	Facing Length (m)	Facing Material	# of Plies per Facing	Tube Type	Purpose
1	0.343	CN60	10	Flattened	Assembly trial
2	0.343	K13D2U	10	Flattened	Thermal prototype
3	1.07	K13D2U	10	Flattened	For modules
4	0.343	K13D2U	3	4.8 mm round/ POCO foam	Thermal prototype
5	0.343	K13D2U	3	2.8 mm round/ POCO foam	Thermal prototype

Table 1 Summary of the prototype staves fabricated.

The principal components of the prototype staves were: facings[*], honeycomb core material[†], aluminum tubes and, for some prototypes, thermally-conducting carbon foam[‡]. The facings were fabricated from the fiber unitape and cured in an autoclave and then cut to the required shape. The honeycomb was pre-cut by the manufacturer to the desired width (two different widths for center and outer sections) and thickness. The carbon foam was machined to the required thickness and shape. The honeycomb pieces were glued[*] to one facing as shown in Figure 5 (left). For prototypes #2 and #3, the aluminum tube was bent and directly attached to a

---

[*] Apart from prototype #1(assembly trial), the facing material was K13D2U Graphite Toughened Cyanate Ester Unitape, 80g per sq m, 6" width, 250°F cure with EX1515 resin.
[†] Material was honeycomb 3/16" cell size, M46J material with epoxy resin. http://www.ultracorinc.com/
[‡] POCO graphite foam with nominal density of about 0.55 g/cc. http://www.poco.com/

facing with a thermally conducting adhesive.[†] For prototypes #4 and #5, the machined pieces of POCO foam were first attached (also with a thermal adhesive) to the bent tube (see Figure 6) and these assemblies then glued to a facing – see Figure 5 (right).
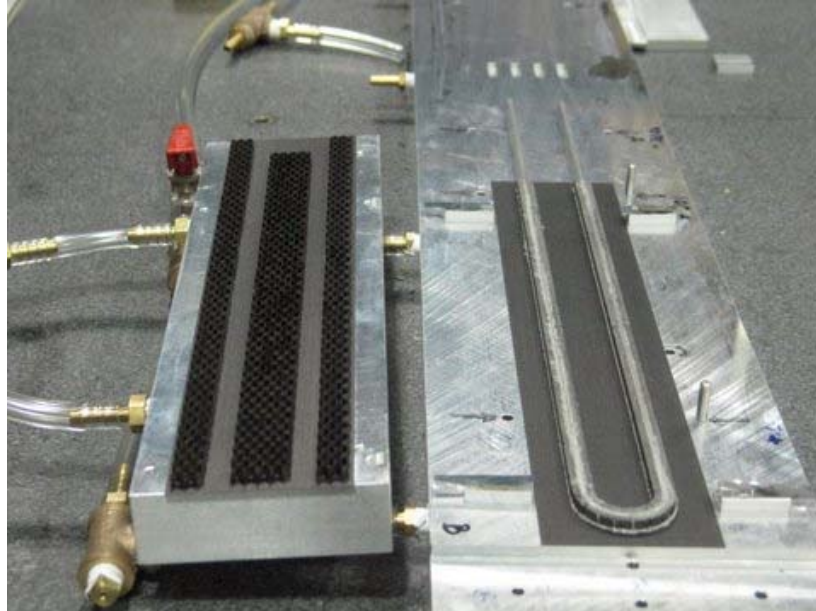
Figure 5 (Left) Honeycomb glued to prototype stave facing. (Right) Round aluminum tube (in this case 4.9 mm OD) surrounded by POCO foam glued to stave facing.

Figure 6 Aluminum pipe (2.8 mm OD) surround by POCO foam pieces, prior to gluing pieces to the tube.

The two half-assemblies were glued together. Additional components were added to prototypes #2 and #3 – side closeouts, consisting of thin machined pieces of facing material and

end-closeouts (machined aluminum) with pins. These components, and the complete prototype #3, may be seen in Figure 7.

Figure 7 Prototype #3 during deflection measurements. The inset shows the detail at one end of the stave.

A photograph of the 1 m – long prototype #3 with the bus-cables attached (on both sides) is shown in Figure 8 and Figure 9.

Figure 8 Photograph of a prototype stave (about 1 m long) with bus-cables attached (to both sides of the stave). The silver strip seen on the left is conducting epoxy to allow for a connection to be made from the end-of-stave card to the facing of the stave. The bus-cable was made in two parts for this prototype.
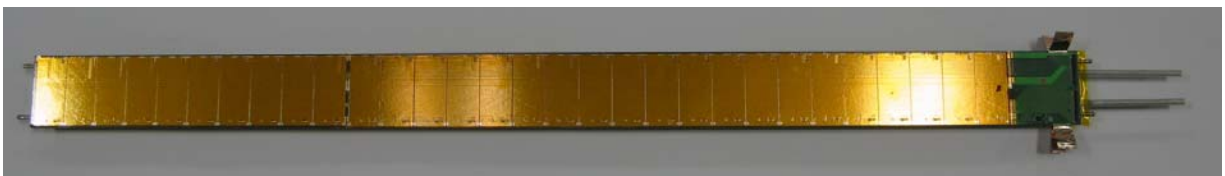
Figure 9 Photograph of prototype stave with end-of-stave cards attached.

2.1 Prototype Thermal Performance

Heaters and dummy hybrids (alumina pieces although BeO would be used in a real detector) and dummy silicon detectors were mounted on a simulated bus cable[*] laminated to each of the three, thermal prototypes – see Figure 10.
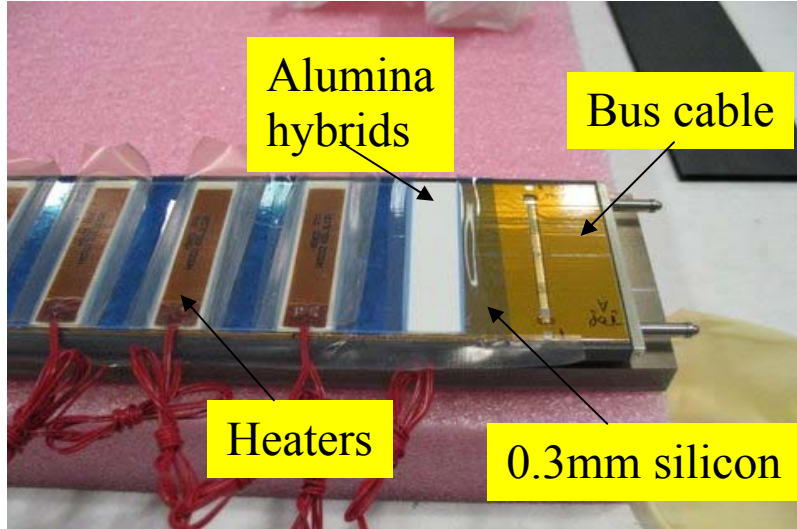
Figure 10 Illustration of the configuration of heaters and simulated hybrids, detectors and bus cable on the thermal prototypes described in the text.
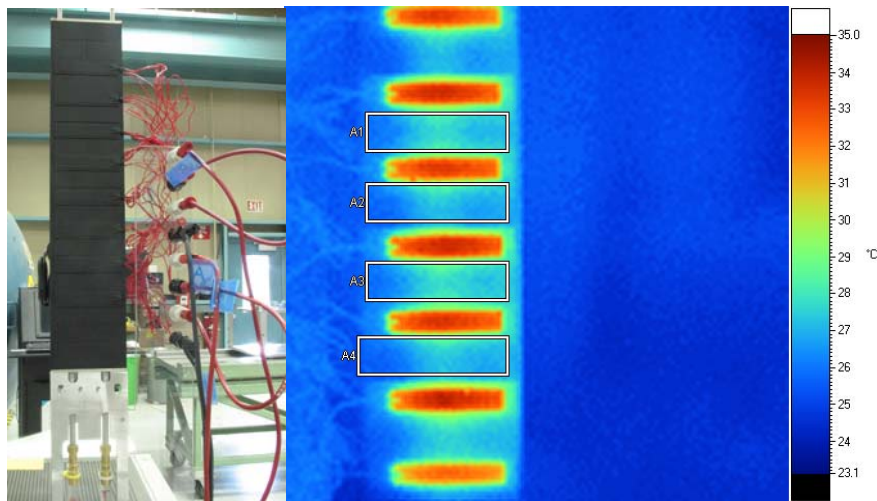
Figure 11 (Left) Configuration of prototypes described in the text for thermal measurements using an IR camera (not shown). Connections to water cooling are shown at the bottom of the photograph. Heaters are powered through the connections shown. (Right) Typical IR image as viewed by imaging software. The minimum, maximum and average temperatures can be obtained in the boxes shown in the figure and were used to characterize the performance.

---

[*] The bus-cable used in the prototypes was intended for use in CDF.

The thermal performance was measured using IR-imaging as shown in Figure 11. Water cooling at about room temperature was used.

We summarize in Table 2 below details of the measurements of the thermal performance of the prototypes prior to thermal cycling. The thermal performance for the three prototypes at a fixed power (3.3 W per hybrid/heater) is given in Table 2. Results obtained at slightly different power values were scaled to 3.3 W per heater assuming a linear dependence of ΔT (the temperature difference between power-off conditions and power-on conditions) in the box regions shown in the Figure 11 (right).

| | Inlet T | Outlet T | Power 1 | Power 2 | 0 pwr T | T min | T max | T ave | Relative to ave water | | | Relative to 0 pwr | | | |
									DT min	DT max	DT ave	DT min	DT max	DT ave	
K13D2U flat tube	20.1	20.6	26.306	26.432	21.4	25.6	29.3	27.34	5.3	9.0	7.0	4.2	7.9	5.9	Looking at side A(pwr 1)
K13D2U flat tube	20.1	20.6	26.404	26.502	22.55	25.3	29.2	27.14	4.9	8.8	6.8	2.7	6.6	4.6	Looking at side B(pwr 2)
K13D2U flat tube	20.1	20.4	0	26.502	20.9	24.8	28.6	26.65	4.5	8.3	6.4	3.9	7.7	5.7	Looking at side B(pwr 2)
POCO 4.8 tube	20.1	20.3	26.264	0	20.6	22.9	26.4	24.61	2.7	6.2	4.4	2.3	5.8	4.0	One side only
POCO 2.8 tube	20.3	21.1	26.404	26.6	20.38	24	28.1	25.62	3.3	7.4	4.9	3.6	7.7	5.2	CGL side
POCO 2.8 tube	20.3	21.1	26.418	26.614	20.3	24.3	28.8	26.02	3.6	8.1	5.3	4.0	8	5.7	EG side

Table 2 Measurements of the thermal performance of the prototypes at 3.3W/hybrid. The temperature differences (DT in the table) between the power on temperatures relative to the average water temperature and to the zero power temperature observed with IR camera are given.

The inlet and outlet temperatures of the water were measured by sensors located in the water flow. The power values given in the table are for each side of the prototype and for eight heaters. The 0 power T value is obtained from the relevant IR image at zero total power. We recognize that these values are systematically higher than the inlet water temperature. This is either from difference in calibration of the sensors and IR camera or from a small heat exchange with the ambient temperature (also close to 20C). The Tmin and Tmax values are taken as the minimum and maximum values, respectively, in boxes (typically four boxes) as shown in Figure 11(right). The ΔTs are calculated with respect to the average water temperature and with respect to the zero power temperature measured by the IR camera. The former are systematically higher, because of the difference between the direct measurement of the water temperatures and the IR measurement at zero power. These differences, about 1 C, give a rough estimate of the systematic error in the absolute ΔT. The uncertainty in the relative ΔT among the different prototypes is less than $1^{\circ}C$. Prototype #4 had heaters on only one side. Single-side measurements of prototype # 5 were not done.

The principal differences between the prototypes are the types of tubes (see Figure 12) and the facing thickness. The tube for prototype #2 was flattened and just the flat faces make contact to the facings through a compliant, thermally-conducting glue interface. The round tube for prototype #4 is surrounded by thermally-conducting, carbon foam, which in turn is bonded to the facings with CGL-7018 adhesive. The smaller, round tube in prototype #5 is surrounded completely by POCO foam. In this prototype, one side of the foam is bonded to the facing with CGL-7018 and the other side with a different, less compliant, thermally-conducting adhesive (there is no significant difference between the ΔT measured for the two sides).*
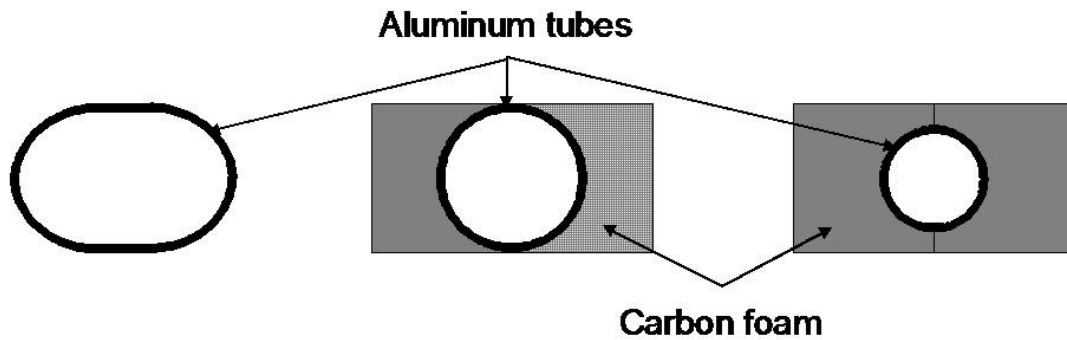
---

* EG7658 from AI Technology.

Figure 12 Illustration of the differences in tube size and shape among the three prototypes measured for thermal performance. Not to scale.

The thermal performance of the three prototypes is similar. The difference in ΔT between single-side and double-side heating is not pronounced. Most the heat is coupled to the tube wall closest to the side under power. However, the performance of the larger round tube with POCO foam is somewhat better than the flattened tube. We attribute this (based on calculation) to better coupling of the heat from the facing through the foam to a greater area on the tube. The smaller tube has a thermal performance similar to the flattened tube. Although heat is coupled better for the smaller round tube, it is a greater distance from the facing, thereby increasing ΔT.

The three prototypes were cycled in temperature from room temperature to -35°C about 50 times and the thermal performance measured again. There was no significant difference in any case between the performance before and after thermal cycling. In particular, no evidence for reduced coupling between the tube and facing for any of the three prototypes was observed.

2.2 Prototype Detector Removal

An important requirement is to be able to remove a detector module from a stave and replace it with another module. In order to evaluate the feasibility of this possibility, a number of silicon pieces, including 6 x 6 cm^2 dummy detectors, were glued to a prototype bus cable surface with a compliant, thermally-conducting adhesive.[*] The adhesive was allowed to cure (in some case up to about one month) and then the dummy silicon was removed and the area cleaned. In all cases, with this adhesive, removal and clean up sufficient to allow replacement was possible. A photograph just after removal of a piece of dummy silicon, but before clean up is shown in Figure 13.
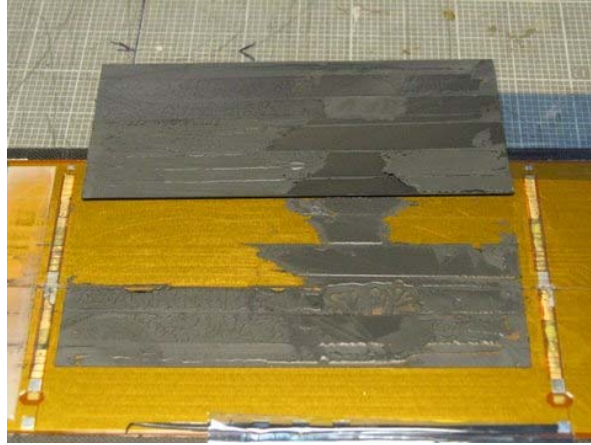
---

[*] SE4445 from Dow Corning.

Figure 13 Photograph of a dummy silicon detector glued with SE4445 just after removal of the dummy detector but before clean up of the bus cable areas.

2.3 Prototype Construction Accuracy

The long prototype (1 m) was surveyed using a precision coordinating measuring machine. The reference system for the measurements was determined by three, precision pins. Two of these pins were located at one end of the stave and one at the other (along with a fourth pin). The estimated placement accuracy of these pins is about 50 microns (determined by the survey of the fourth pin) in the plane of the stave. The surface of the prototype stave was scanned with a touch probe and many hundreds of points measured (in the defined coordinate system). Scans by the touch probe across the short-dimension of the stave were taken at intervals along the length. The flatness of the surface may be assessed from Figure 14. One can see that all points are within a band about 200 microns wide. The rms of these points is about 31 microns. A scan of the other side of the stave also indicates that all points are within a 200 micron-wide band but with an rms of 55 microns. The deviations from flatness were primarily caused by changes in the thickness of the honeycomb in different regions of the stave. This effect could be reduced by precision grinding of the honeycomb (not done for these prototypes).
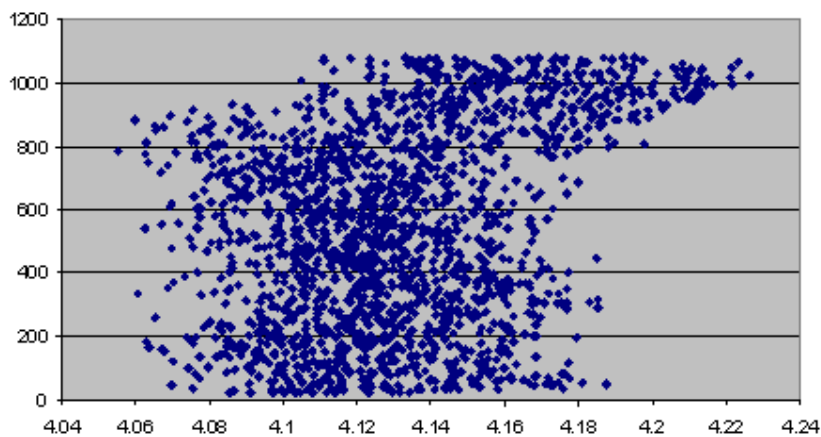

Figure 14 Measurements of the flatness of one side of the 1m-long prototype stave. The length along the long direction of the stave is given on the vertical axis (in mm). The location of the surface, relative to the coordinate system described in the text, is shown on the horizontal axis (in mm). Scans across the short-dimension of the stave were taken at intervals along the length.

2.4 Prototype Weights

The measured weights of the prototypes are summarized in Table 3. These weights are used as input to the estimates of the radiation length for stave designs described in a later section.

Prototype # --->	2	3	4	5
Principal elements	10 plies Flattened tube	10 plies Flattened tube	3 plies 4.9 mm/foam tube	3 plies 2.8 mm/foam tube
Facing length(m)	0.343	1.07	0.343	0.343
Facings	51.44	160.44	16.36	16.21
Honeycomb	4.61	15.62	4.18	4.19
Tube (bare)	12.56	35.49	11.76	7.04
Foam	0	0	6.88	12.91
Thermal adhesive	3.18	10.56	9.78	6.46
Epoxy	6.25	15.72	4.69	5.37
Subtotal	78.04	237.83	53.65	52.18
Side closeouts	9.17	27.30	0	0
End closeouts	20.82	24.43	0	0
Total	108.03	289.56	53.65	52.18

Table 3 Measured weights in grams of the principal components of the prototype staves.

3. Coolant Tube Sizing and Two-Phase Flow

We have assumed evaporative cooling as a basis for our design. However, the type of evaporative coolant has not been selected for the SLHC. It is, therefore, important to understand the implications of alternatives for the evaporative fluid. It also important to recognize that estimates of performance with evaporative cooling must be substantiated ultimately by measurements of realistic prototypes.

The fluid enters the cooling tube (2m path length for a 1m stave length) as a mixture of liquid and vapor with a quality (vapor fraction) in the range of .05 to 0.1. The two-phase fluid is heated convectively throughout the 2 meter passage length, exiting with a quality approaching 0.85. An exit quality < 1 is essential to ensure a "dry-out" condition does not occur, since heat transfer to a super-heated vapor results in a rapid rise in detector temperature.

These stated inlet and exit qualities, a measure of the amount of vapor present, should be considered nominal. However, the difference between the two numbers and the latent heat of evaporation of the fluid set mass flow requirements to absorb the detector heat load.

In absence of a pressure change, phase change from liquid to vapor occurs at constant temperature.   Hence, one can imagine the fluid entering at, for example, -25ºC and leaving without a temperature change, with zero pressure drop. In reality, the flow through the stave results in a decay in saturation pressure. A lower saturation pressure leaving corresponds to a lower saturation temperature, leading to a colder exit fluid, while the phase change removes

upwards of 240W for the 2m transit. Hence, the stave inlet pressure in this situation less by the amount of the pressure drop.

P.B. Whalley is a good reference for calculation of flow-boiling heat transfer.[3] This reference covers nucleate boiling and convective boiling. Nucleate boiling is characterized by bubbles forming at nucleation sites on the tube wall. Convection boiling corresponds to heat transfer by conduction through a liquid film, followed by evaporation at the liquid-vapor interface. Both forms can co-exist, but as quality increases the dominant contribution becomes convection boiling in most instances.

Whalley, and others, account for heat transfer with two contributions, an element associated with nucleate boiling and flow-boiling. He attributes the work to Chen.[4] In this way the contributions work in parallel;

$h_b = h_{nb} + h_{fc}$, where the subscripts for the individual contributions denote boiling, nucleate boiling, and flow convection. The nucleate boiling expression is;

$h_{nb} = S h_{F-Z}$, where S is a suppression factor applied to the nucleate-boiling heat transfer calculated from the Forster-Zuber equation,

$$h_{F-Z} = \frac{0.00122 \Delta T_{sat}^{0.24} \Delta P_{sat}^{0.75} C_{pL}^{0.45} \rho_L^{0.49} k_L^{0.79}}{\sigma^{0.5} \lambda^{0.24} \mu_L^{0.29} \rho_v^{0.24}}$$, where the subscripts L and v denote liquid

and vapor fluid conditions. The difference between the tube wall and saturated fluid is ΔT_{sat} and the associated change in saturation pressure for this temperature differential, which in turn gives rise to bubble formation, is ΔP_{sat}. Fluid properties, Cp, ρ, k, σ, λ, and μ, are specific heat, density, thermal conductivity, surface tension, latent heat of evaporation, and viscosity respectively.

The convective heat transfer coefficient h_{fc} is based on a modification of an expression used in single phase heat transport. $h_{fc} = h_L F$, where h_L is the single phase (liquid) convective film coefficient based on standard Reynolds and Prandtl number correlations. Here, Whalley chooses the familiar Dittus-Boelter equation:

$$Nu_L = 0.023 \, Re_L^{0.8} \, Pr_L^{0.4}$$

However, in two-phase flow the Reynolds number is a function of the fluid quality.

$Re_L = \dfrac{G(1-x)D_h}{\mu_L}$. G is the product of fluid density and flow velocity, χ the flow quality,

and D_h the hydraulic diameter of the passage.

To obtain h_{fc} we must know h_L. h_L is obtained from the definition for Nu_L:

$$h_L = \frac{Nu_L k}{D_h}$$

However, to obtain Nu_L we must first evaluate S and F. Chen's contribution was to suggest ways to obtain expressions for S and F. In Whalley, Chen's curves for S and F exist as a function of the Reynolds number for two-phase flow (Re_{TP}):

$Re_{TP} = Re_L \, F^{1.25}$,where F is a heat transfer multiplier.

To obtain "F" the procedure uses the Martinelli parameter X . Chen assumes that the friction of each phase is proportional to $Re^{-0.2}$ leading to:

$$X = (\frac{1-x}{x})^{0.9} (\frac{\rho_v}{\rho_L})^{0.5} (\frac{\mu_L}{\mu_v})^{0.1}$$

This value is an entry into a figure for F in Whalley. So one must calculate F first and then use F to calculate Re_{TP}. S is obtained from a figure correlating S with F. It is worth mentioning that explicit relationships for S and F can be found in Krieth that streamlines the process a bit once values of X and Re_{TP} are known.[5]

Reviewing the above, we see that the convective term is a function of Reynolds and Prandtl numbers, which in turn is a function of fluid quality, mass flow and the hydraulic diameter, not to mention fluid properties. Calculation of this contribution does not require iteration. However, the calculation of the boiling contribution does. To arrive at the boiling film coefficient one must have a heat balance across the film that includes both convective and boiling heat transfer. So the process is: for a given heat flux, calculate the convective film coefficient; for boiling one assumes a ΔT_{sat}, which fixes ΔP_{sat} (along fluid saturation boundary), and with the two components one calculates the film temperature gradient using the assumed heat flux. This calculated film temperature gradient must agree with the assumed ΔT_{sat}, within a reasonable error. As required, one iterates until an energy balance is achieved.

We used the two-phase flow analysis procedure discussed above to calculate the effective film coefficient and film temperature gradient for both C_3F_8 (Figure 15) and CO_2 (Figure 16).[6] The prescribed conditions for a 1m length stave (2m U-tube) were -25ºC for C_3F_8 and -35ºC for CO_2, both accepting 240W of thermal heating while changing from inlet quality of 0.05 to an exit quality of 0.85.

Figure 15   Plots of heat transfer coefficients and film temperature drop for C_3F_8, based on a 4.29mm ID tube with 240W in a 1m stave length (2m tube length).

One may notice that the effective film coefficient for each is low at low vapor quality, increasing as fluid evaporates and vapor quality increases (higher fluid velocity). The convective term is responsible for this increase; as one can see the boiling contribution is decreasing with increased vapor quality.
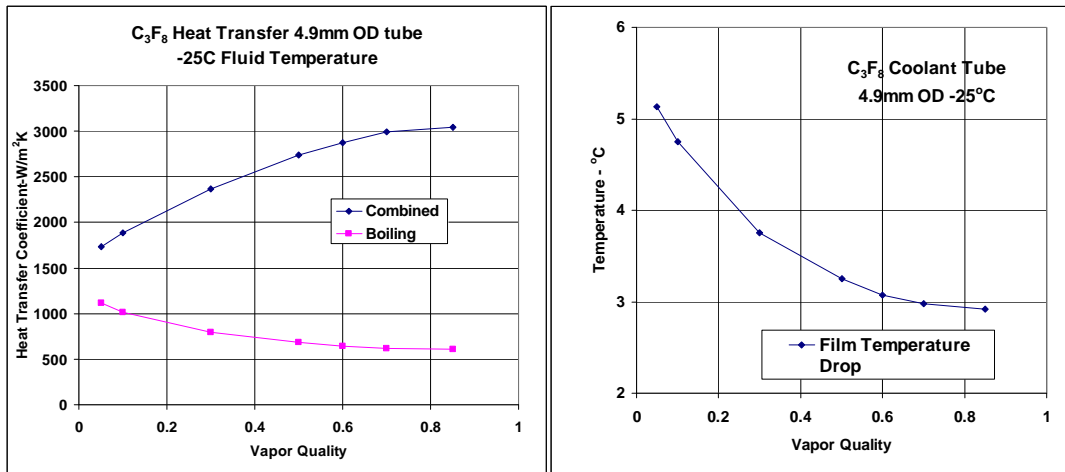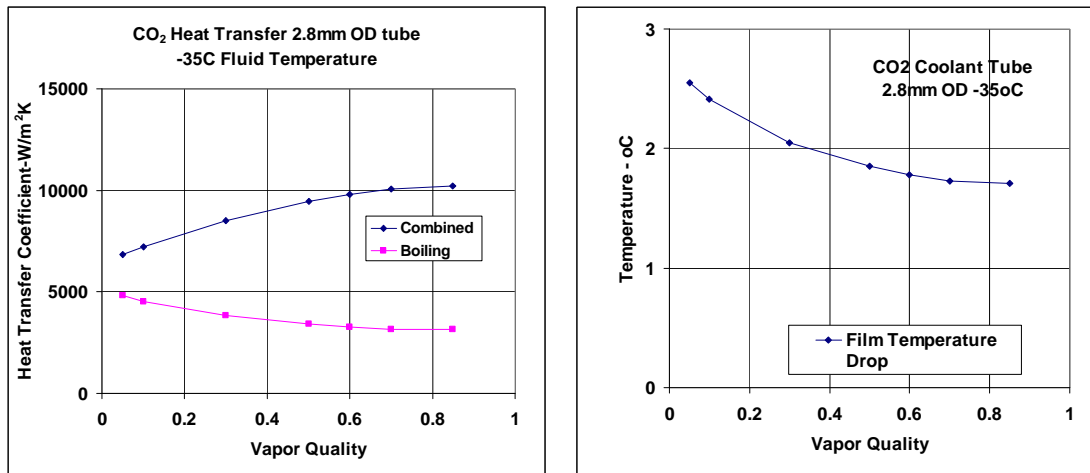
Figure 16 Plot of heat transfer coefficients and film temperature drop for CO_2, based on a 2.19mm ID tube with 240W in a 1m stave length (2m tube length.

The temperature gradient through film is much higher for C_3F_8 than for CO_2, particularly at the entrance of stave, suggesting that this will be the most likely region for thermal runaway to occur. One question that first comes to mind is to what extent the highly conductive materials in the stave will cause some re-distribution of heat transfer, lowering the heat flux regionally and smoothing out the film temperature curve. It is felt that the small length-wise gradient, 2 degrees for C_3F_8, and less than a degree for CO_2 make this fairly remote. Thus, we choose to use the effective film coefficients near the entrance of the stave for estimates of headroom against thermal runaway.

We have calculated the ΔT from the film coefficient in the fluid (at the entrance to the stave) and from the change in pressure around the cooling loop, since the evaporation temperature depends on pressure. The results for CO_2 and C_3F_8 coolants are given in Table 4.[6] These calculations were done for a total power of 240 W for a 1 m stave length. The path length for the simple U-Tube is 2m and 4m for the Triple U-Tube cooling loop. The assumed values for the entering and exiting flow quality are 0.05 and 0.85 respectively. The pressure drop is fairly sensitive to these values. For example, assumptions of 0.1 and 0.8 would increase the mass flow and in turn the pressure drop by roughly 25% (213mbar versus 170mbar). A similar percentage change occurs in the ΔT (Loop) 3.1ºC versus 2.5ºC.

Fluid	Tube OD (mm)	Tube ID (mm)	Hydraulic Diameter (mm)	ΔP (mbar)	Coolant (ºC)	ΔT(film) (ºC)	ΔT(loop) (ºC)
C_3F_8 U-tube	4.9	4.29	4.29	170	-25	5.2	2.5
C_3F_8 U-tube	4.9(oval)	n/a	5.27	59	-25	4.0	1.0
C_3F_8-Triple	4.9(oval)	n/a	5.27	110	-25	3.2	1.6
CO_2 U-tube	2.8	2.19	2.19	675	-35	2.5	1.0

Table 4 Calculations of the pressure drop (ΔP) around the cooling loop and of the ΔT (at entrance to stave) values from the film coefficient and around the loop as described in the text for different tube diameters and coolant fluids.

– 14 –

One observes that the ΔP (and the resultant ΔT around the loop) is sensitive to the tube diameter. If one assumes the current performance of the C_3F_8 system installed in ATLAS, namely minimum coolant temperatures at the exhaust-end of a stave of about -25°C, then a hydraulic diameter about 5 mm would be required. However, if the system could be reconfigured to allow lower temperature operation or if mixtures of fluorocarbons allow lower temperature operation, then perhaps hydraulic diameters 4.5-5 mm might be allowable. Evaporative cooling with CO_2 potentially allows for significantly smaller tube hydraulic diameters, 2-2.5 mm, and colder fluid operation. This would have the practical effect of relaxing the requirements on the thermal conductivity of the stave sub-components and significantly reducing the material (radiation length) of a stave.

In subsequent sections, we present calculations of the ΔT predicted for different stave structures and estimates of the effect of "thermal runaway" from detector self-heating after radiation damage. We typically plot ΔT as a function of the tube wall temperature but the reader should keep in mind that there are additional ΔTs arising from the effects summarized in Table 4 and that these effects depend sensitively on the coolant type, heat loads, heat transfer coefficients, pipe diameters, etc. There will inevitably be some level of uncertainty in the calculations that can only be reduced by careful measurements of full-scale prototype structures with a given coolant under carefully controlled conditions.

4. Modeling Thermal Performance

In this section we describe estimates of the thermal performance of the integrated stave. We first describe briefly the thermal models constructed to compare with the thermal prototype measurements presented previously. We then summarize our assumptions about some of the key input heating parameters (silicon detector self-heating, electronics power and others) for the full-size stave. We then present estimates of the thermal performance of a full–size stave, including thermal runaway. The effects on thermal performance from variations in input assumptions and changes in the composition of the stave are also given.

4.1 Thermal Prototype Modeling

Finite element models of the thermal prototypes were constructed to compare with the measurements and to assist in the validation of the modelling process. These models were similar to those described in more detail later for the full-size stave. The models include all elements of the prototype staves (alumina, silicon, bus cable, facings, tubes, thermally conducting foam, if applicable, glue interfaces, etc). An example illustration of the output of a model is given in Figure 17. The observable maximum "silicon" temperature in this example is 27.5^{o}C, or a ΔT of 7.5^{o}C, to be compared with the measurement (Table 2) of 7-8°C for thermal prototype #2 (difference from 0 power temperature). A model applicable to thermal prototype #4 yields a maximum temperature of 5-6 degrees (depending upon differing assumptions about the thermal conductivity of facings, foam, etc) to be compared with the measured maximum of about 6°C given in Table 2 . In general we found agreement between measurements and model predictions within about 1°C. However, it must be noted that absolute error in the measurement is also about 1°C. In addition, the values of the thermal conductivity of the prototype stave components are not well enough known to be able to predict the temperatures to an accuracy better than about 2°C to compare with the measurements. Thus, while the agreement between the models and the measurements is reasonable, it should be remembered that uncertainties in the range of about 1-2°C are present.
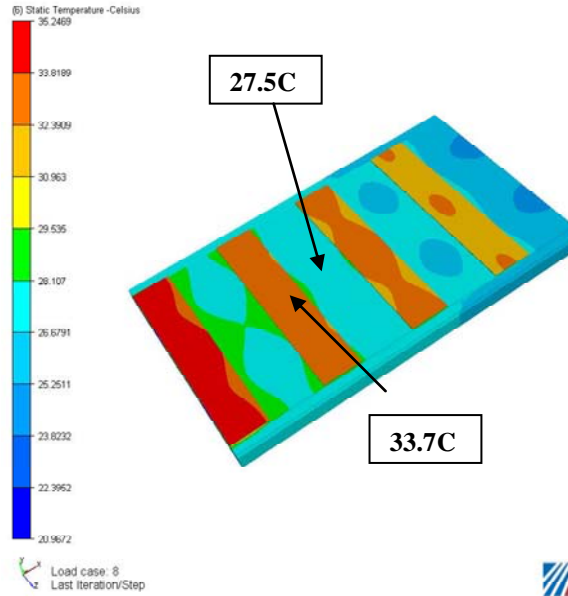
Figure 17 Model predictions for 3.3W per hybrid, 20C cooling water at 1.27 liter/min and double-sided heating for a semi-flattened tube prototype stave.

4.2 Heating Parameters

The heat loads on the stave arise from the electronics mounted (on hybrids) on the stave, from silicon detector heating (from the leakage current that varies with the amount of radiation damage and voltage), from resistive heating in the bus cable and from heat loads from the ambient environment of the stave. In general, we have not included the last item in the models (with the exception described in 4.6). The nominal value assumed for the heat load from the electronics is taken to be the equivalent of 0.3 W per front-end chip. Thus, in the case of the short-strip detectors, the nominal heat load from the electronics on one side of the stave per meter is approximately 0.3 x 10 (chips per short detector segment) x4 (short detector segment per 10 cm long detector) x 10 (detectors per meter) = 120 Watts. We have looked at the consequences of lower electronics power (0.125 W per chip) and more electronics power (0.5 W per chip).

The detector self-heating has been taken from a parameterization[7] that assumes a total integrated luminosity of 6000 fb[-1] (which would roughly correspond to six years at an average luminosity of 10^{35} cm^{-2}sec^{-1} or alternatively a lower integrated luminosity e.g. 3000 fb[-1] with a safety factor of two for uncertainties in radiation levels and other factors). The value of the self heating is for a radius of about 30 cm, about the lowest radius currently anticipated for silicon strip detectors in an upgraded detector in ATLAS. Numerically, the self-heating is about 1 mW/mm^2 at 0°C. We have looked at the consequences for higher values, as shown later.

The power dissipation in the bus cable depends very significantly on the scheme for powering hybrids e.g. how serial powering is implemented. Effectively we have assumed that the bus cable design will be such as to make the power dissipation in the bus cable low i.e. < 10% of the electronics power and therefore we have neglected this contribution in the calculations presented below.

4.3 Model for Preliminary Thermal Runaway Estimates

In the 10 cm wide module design, there are 10 electronic chips per each hybrid. There are 4-hybrids per 10 cm module. This arrangement is configured in the finite element (FE) model as a 2.5cm long unit with 5chips (1/2 width model), with the stave middle being a plane of symmetry. The final plane of symmetry is the mid-plane of the cooling tubes, making overall a ¼ actual size model. We have chosen to model only one variant of three possible tube configurations – a small diameter tube surrounded by thermally conducting foam. This configuration would be typical for CO_2 coolant. We note that the thermal performance, as measured by the ΔT between the coolant and the hottest spot on the silicon seen in the thermal prototypes, was somewhat better (but only by about $1^{o}C$) for a larger diameter tube partly surrounded by thermally conducting foam, a configuration more applicable to C_3F_8. We also note that the thermal performance of a flattened tube, as seen in the prototypes, was similar to the small-tube configuration. Thus, we expect the model to be representative of the thermal performance, as measured by ΔT from the tube inner wall to the silicon detectors, for CO_2 and C_3F_8 (or mixtures with C_3F_8) but the effects of pressure drop around the cooling loop and the film coefficients must be taken into account for each fluid.

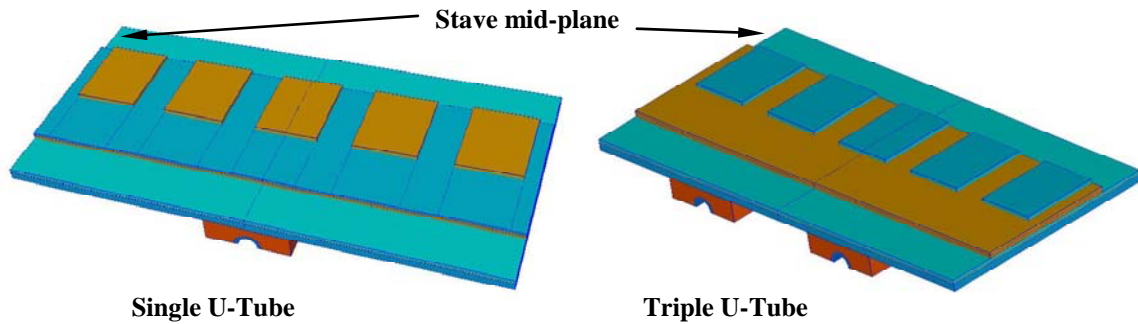**Single U-Tube**   **Triple U-Tube**

Figure 18 Finite elements model for (left) single U-tube and (right) triple U-tube as described in the text.

The cooling tubes in this study run in the stave axial direction with a symmetrical transverse spacing dependent on the number of back-forth coolant passages). For a single U-tube (down once and back) the stave lateral dimension is divided into two equal transverse thermal zones with respect to the chips. Each cooling tube is thus placed ¼ of the distance from the outboard stave edge. A geometry with a triple U-tube cooling tube makes four passes. The single- and triple-U-tube models are shown in Figure 18.

The FE baseline parameters used in the estimates of thermal runaway using this model are illustrated in Figure 19 and summarized in Table 5. Global coordinates are X (transverse to stave long axis), Y (normal to stave surface), and Z (stave axis). Unless otherwise noted the properties are isotropic.
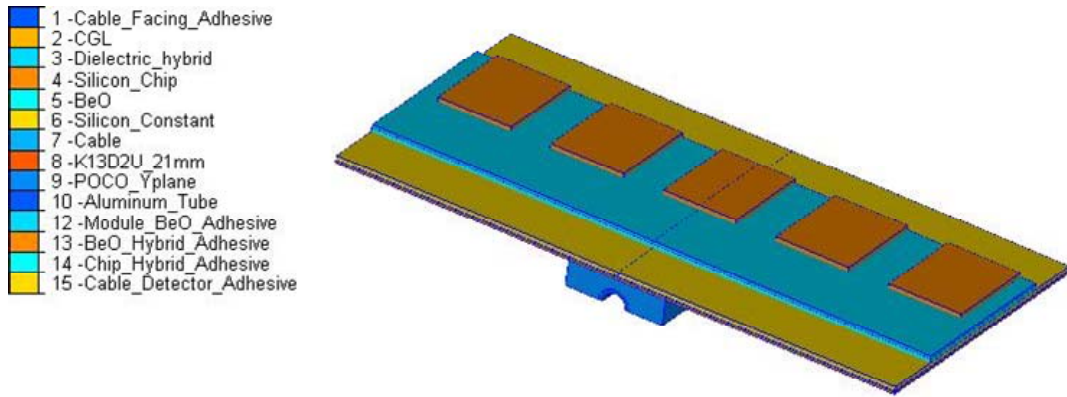
Figure 19 FEA model used in CFDesign to calculate the thermal gradient from chip to the single U-Tube that is bonded to the composite facing through a POCO foam saddle.

Item	Thickness	Thermal Conductivity (W/mK) X/Y/Z
Solid Elements		
Tube OD: 2.8mm, ID: 2.1mm		200
Composite Facing Thickness	0.21mm	148/1.3/294
Cable	0.125	0.12
Detector	0.28mm	148
BeO	0.38mm	210
Dielectric Hybrid	0.23mm	5
Chips	0.38mm	148
POCO Foam (0.9mm min)	varies	50/125/50
Adhesives		
Foam to Tube (CGL)	0.1 mm	1
Foam to Composite Facing (CGL)	0.1 mm	1
Facing to Cable	0.05 mm	0.8
Cable to Detector	0.05 mm	0.8
Detector to BeO	0.05 mm	0.8
BeO to Dielectric hybrid	0.05 mm	1.55
Dielectric to chip	0.05 mm	1.55

Table 5 Baseline properties used in the finite element model described in the text.

4.4 Thermal Results

The estimates of temperature are determined by iteratively running the FE model at different tube inner wall temperatures for different assumptions about the heat input parameters. The results for the peak detector temperature are summarized in Figure 20 for the single U-Tube. The results for no silicon detector heating are included for reference. The results for a triple U-tube are shown in Figure 21.
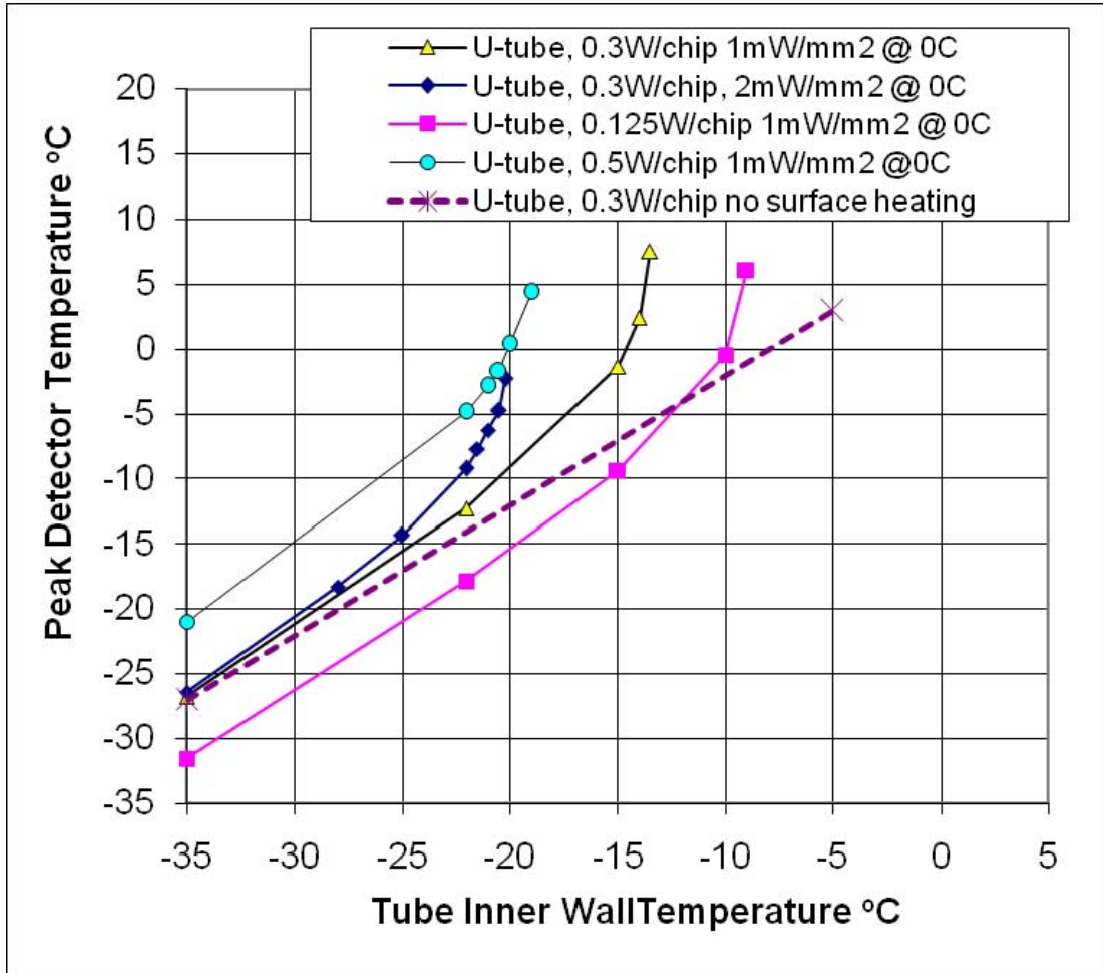
Figure 20 Peak detector temperature versus inner wall temperature of the coolant tube for different heating conditions for a single U-tube coolant pipe using the model described in the text.

It is apparent from these results that the baseline design with a single U-tube and with C_3F_8 cooling with $T_{min} \sim -25^{o}C$ has marginal headroom against thermal runaway. We have studied the effect of changing the facing composition, of improving the thermal performance of the bus-cable and of replacing the honeycomb with low-density, thermally conducting, carbon foam. These calculations are described in the next sections.
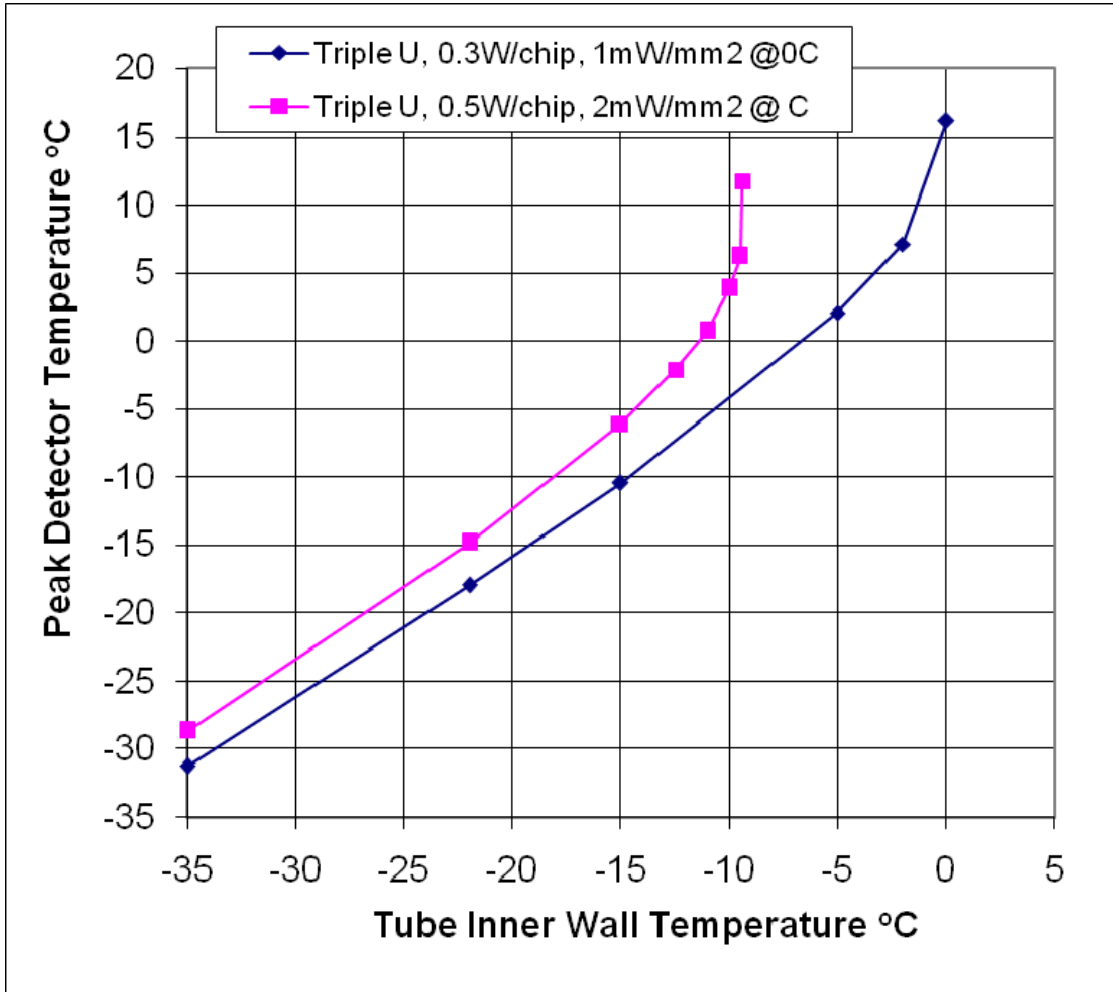
Figure 21 Peak detector temperature versus inner wall temperature of the coolant tube for a triple U-tube configuration using the model described in the text.

4.4.1 Facing Composition Variations

We have looked at the effects of varying the parameters (layup and thickness) of the facings assuming the facing material is K13D2U, the effect of using a fiber (K1100) with somewhat higher thermal conductivity and of using carbon-carbon facings that would have significantly higher thermal conductivity through the facing. The studies of facing in variations are summarized in Table 6.

Table 6 was constructed via individual FE solutions using a 0ºC cooling tube inner wall surface as a reference temperature, thereby providing a ready display of the gradient from the detector or chip to the tube inner surface. Facing thickness values are predicated on the basis of the final thickness for the chosen fiber orientations (layers). A concentration of fiber in the stave longitudinal direction (Z in this case) is chosen to favor higher stave stiffness in this direction.

Facing Properties Fiber K is given (Z/X/Y)	Thickness (mm)	Lay-up	Chip Peak ΔT (ºC)	Detector Peak ΔT (ºC)	Cooling Tube
K13D2U(294/148/1.3)	0.21	0/90/0	8.61	7.96	Single U-Tube
K13D2U(221/221/1.3)	0.42	0/60/-60/s	7.31	6.61	Single U-Tube
K13D2U(294/148/1.3)	0.42	90/0/0/s	7.93	7.24	Single U-Tube
K13D2U(352/89/1.3)	0.70	90/0/0/0/0/s	8.30	7.62	Single U-Tube
Carbon-Carbon(314/183/25)	0.42	90/0/0/s	6.88	6.19	Single U-Tube
K1100(367/185/2)	0.21	0/90/0	8.05	7.39	Single U-Tube
K13D2U(386/97/1.44)	0.21	0/90/0	4.34	3.69	Triple U-Tube
K13D2U(352/89/1.3)	0.70	90/0/0/0/0/s	5.25	4.55	Triple U-Tube

Table 6 Effects on thermal performance from variations in the facing properties assuming a 0ºC temperature for the coolant tube inner wall, 0.3 W/chip and no detector heating.

Very thin composite facings are planned using a 3-layer construction with a fiber orientation 0/90/0 (as was used in some of the prototype fabrication). Three examples of this thin facing are compared, K13D2U versus K1100 with a single U-Tube and K13D2U with a Triple U-tube. One may note that the K1100 fiber thermal conductivity (Z) is higher (>25%) than K13D2U, yet there does not appear to be a thermal justification to select it over K13D2U; particularly since K13D2U's tensile modulus is within 5% of K1100. In the case of the K1100 fiber, a slight improvement in the single U-Tube performance 7.39ºC versus 7.96 ºC is realized. A symmetric layup (0/60/-60/s) would yield slightly better thermal performance but with more material. Using more costly carbon-carbon material[*] for the facings would improve the performance by about 1.8ºC compared to the K13D2U baseline. A clear advantage favors the Triple U-tube in minimizing the detector surface temperature over the single U-Tube, as one expects, 3.69ºC versus 7.96 ºC.

4.5 Extended Thermal Model

An extended thermal model was created to represent the 10cm wide stave in more detail. This model was extracted from a 1meter long solids model of the complete stave. Length-wise this thermal model represents a single 10cm wide by 10cm long detector module, back-to-back. There are four rows of chip, 10 across for a total of 80 chips (both sides). The composition of materials and breakdown of material thickness is the same as listed in Table 5. There are two differences with respect to the ¼ FEA model of Figure 19. One, this model has composite side close-outs for the sandwich (no effect on the thermal performance) and two, a foam core replacing the honeycomb assumed for the ¼ model. The side-close out is of the same composite material as the composite facing. And the foam core thermal conductivity is considered as a variable, ranging from 15 to 45W/mK.

---

[*] We also note that carbon-carbon is available in panels of limited size and thus the facings would be made from a number of pieces.

Since this model consists of multiple chip rows and many more elements (~1.6million finite elements) it is therefore much computationally intensive in temperature dependent heating solutions, like what is needed for thermal runaway calculations. Whereas each solution point (reference Figure 21) for the ¼ model was obtained in a few minutes, each temperature dependent solution of this model takes several hours. A complete solution for the entire temperature domain from -35ºC to point of thermal instability with this model requires most of a day. Addition of the sandwich core contributed to this computational problem. A sample steady state solution is illustrated in Figure 22.
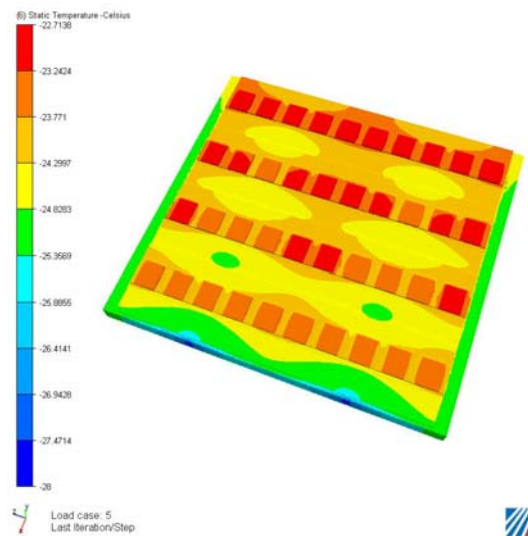

Figure 22 Illustration of a more complex thermal model described in the text.

4.5.1 Comparison of Models

The 10cm by 10cm FE model was compared with the simpler ¼ size model used in initial thermal runaway estimates, by setting the foam core thermal conductivity in the more complex model to an extremely low number ($5*10^{-5}$ W/mK). The ¼ FE model assumed honeycomb core with negligible thermal conductivity, consequently a representation for this material did not exist in the previously reported thermal performance. To place the comparative solutions on a common footing both models used the same material properties throughout (K13D2U at 0.21mm) with the exception of the foam core. An inner tube surface of -22ºC was used, with detector surface heating included and a 0.3W/chip heat load. In comparing the peak detector surface temperature for both (same nodal region), we found -12.17ºC for the 10cm by 10cm model and -11.76ºC for the ¼ model, which provided comparative results within 0.41ºC. This agreement is considered good, considering the higher mesh density and addition of the side close-outs in this new model. In short, the more complex model without the conductive foam core yields essentially the same thermal result within about 0.5°C.

The sensor temperature uniformity can also be obtained from the more complex model. The sensor temperature uniformity is about 3°C (from coldest to warmest) when operating near the T_{min} of the fluid for the nominal heating parameters, 0.3 W/chip and 1 mW/mm^2 @ 0°C.

4.5.2 Bus-cable Variations

Thermal studies for the stave have addressed both a 7cm wide and a 10cm wide configuration with a very thin, laminated kapton bus-cable sandwiched between the detectors and the composite stave facing. In both configurations, over most of the stave surface, the cable lamination is largely kapton, with layers of copper, and aluminum interspersed on a portion of the stave width. This arrangement results in variable cable conductivity. In the region where laminations of copper and aluminum are present, the cable conductivity, both through-the-thickness and in-plane, are increased. We estimate for a cable lamination of copper and aluminum that locally the K (thickness) to be 0.38W/mK. In-plane, the local thermal conductivity may be upwards of 80W/mK, but this strongly depends upon to what extent the aluminum and copper planes are continuous. In order to be conservative, the thermal stave modelling used an isotropic value of 0.12W/mK (typical of kapton) for the bus-cable in the detailed model shown in Figure 22, with a cable thickness of 125microns. We note that changing the K from 0.12 to 0.38 W/mK, would result in a ΔT improvement of about 1.5°C. Substrate materials other than polyimide are potentially available with significantly higher thermal conductivity. A development area for the bus cable design would be to understand the feasibility of using these materials to improve the thermal performance whilst retaining the high-voltage characteristics and other desirable features of polyimide with the goal of raising the conductivity to $\sim$ 1 W/mK.

4.5.3 Thermally Conducting Foam vs. Honeycomb

We have estimated the improvement resulting from replacing the honeycomb with low density, thermally-conducting carbon foam with K=15 W/m-K.[8] In this model, the low-density foam (0.1-0.2 g/cc) only replaces the honeycomb and the higher density foam is retained around the coolant tube. Should this option be pursued, one would optimize the overall foam composition to attain the desired thermal performance whilst minimizing the radiation length. The thermal performance of this alternative is illustrated in Figure 23. The addition of the foam gives substantially better thermal performance, since it provides an additional heat conduction path to the coolant tube in addition to the facings. For the nominal heating assumptions (0.3 W/chip and 1 mw/mm^2 @0°C) for a single U-tube, the addition of the foam provides about eight degrees more headroom against thermal runaway. Thus, a design with single U-tube and this foam would have acceptable headroom for thermal runaway for C_3F_8 coolant with T_{min}=-25°C.

4.6 Bridged Hybrid

Hybrids are glued directly to the silicon detectors, which are glued to the bus-cable, in the baseline stave design. An alternative – bridged hybrid – is to glue the hybrid to a separate support, the bridge, which in turn is glued to the stave. A thermal model of this arrangement has been constructed and initial estimates of the thermal performance have been made. We note that the calculations for this option have been done for 0.25W/chip and for a fixed inner wall temperature of -28°C and no detector self-heating. The goal was to compare with the baseline design for the similar assumptions.
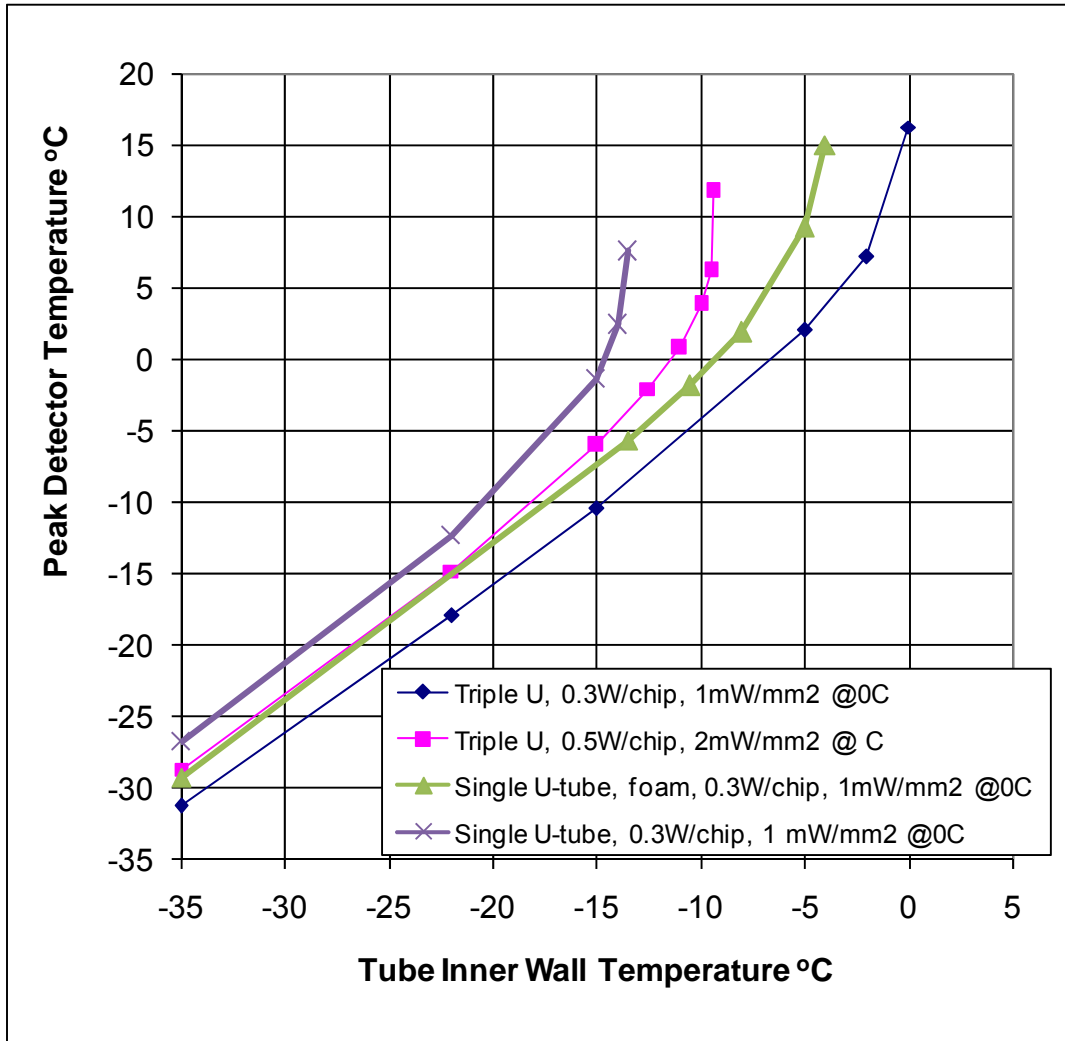
Figure 23 Thermal performance of a stave with thermal conducting foam instead of honeycomb (green triangles). The results (from section 4.4) with honeycomb, and for the given heating conditions, are also included here for comparison.

Table 7 lists the properties of the materials used in the Bridge Model FEA. The Z-axis used in the material definition corresponds to the longitudinal axis of the stave. The sandwich composite facing thermal conductivity presumes a 3-layer 0/90/0 lay-up at 41% fiber fraction. This fraction of fiber was realized in the prototype construction; earlier analyses (described previously) presumed 55% fiber fraction theoretically yielding 148/1.3/294 W/mK. The bridge analysis effort was cut short before a comparative solution could be made at the higher composite facing thermal conductivity. Note also that the conductivity of the bus-cable was taken to be somewhat better than the baseline in this model.

Three types of modules have been constructed to investigate the thermal aspects of this design. The simplest of these is a ¼ model, illustrated in Figure 24. In this model, the integrated circuits are mounted on a kapton hybrid, in turn glued to a thermally-conducting (carbon-carbon) bridge structure that contacts the stave outboard of the silicon detectors, leaving a small gap between the detectors and the bridge. Wire bonds connect the electronics to the detector as shown in Figure 24. In the ¼ model, the effects of air are calculated assuming an air layer only

under the bridge. The 1mm stagnant air gap beneath the composite bridge is represented with solid elements with a thermal conductivity of 0.025W/mK. This high resistance forces the heat to flow across the bridge to the side support point, resulting in a bridge gradient of 6.6ºC.

Item	Thickness	Thermal Conductivity (X/Y/Z W/mK)
Solid Elements		
Tube OD: 2.8mm, ID: 2.1mm		200
Facing (K13D2U-41% fiber fraction)	0.21 mm	110/1/219
Cable	0.125 mm	0.2
Detector	0.32 mm	148
CC bridge	0.5 mm	700/25/25
Dielectric Hybrid	0.23 mm	1
Chips	0.38 mm	148
Carbon Foam for Sandwich	4.9 mm	3
Carbon Foam for Bridge	4.9 mm	45
Carbon Foam for Tube	n/a	45
Adhesives		
Foam Bridge to CC Support	0.050 mm	1
Foam Bridge to Composite Facing	0.050 mm	1
Foam Bridge to POCO Foam	0.050 mm	1
Carbon Foam to Tube	0.050 mm	1
Carbon Foam to Facing	0.050 mm	1
Facing to Cable	0.050 mm	1
Cable to Detector	0.050 mm	1
CC Bridge to Hybrid	0.050 mm	1.55
Dielectric Hybrid to Chips	0.050 mm	1.55

Table 7 Materials and properties used in the study of the bridged-hybrid model.

Our bridge side support attaches to an internal core of conductive carbon (graphitized) foam. This highly conductive foam, sandwiched between the composite facings, provides a direct thermal path to the embedded U-cooling tube. Conductive foam around the tube is also included in this model (as it was in the extended model). And there is foam between the tubes that can have much lower thermal conductivity (and therefore density). Thus, to summarize, there are three types of foam represented in the model:

- bridge foam – from the foot of the bridged hybrid to the foam surrounding the cooling tube
- tube foam – surrounding the cooling tube
- sandwich foam – between tubes/foam, not in direct contact with the foot of the bridge

For the solution depicted in Figure 24, a thermal foam conductivity of 45W/mK was used for the tube foam and the bridge foam, and 3W/mK for the sandwich foam. For this solution, a peak chip temperature at -5.83ºC is noted. Directly beneath this region the detector surface is -20ºC, with a low of nominally -23.3ºC near the outside edge.
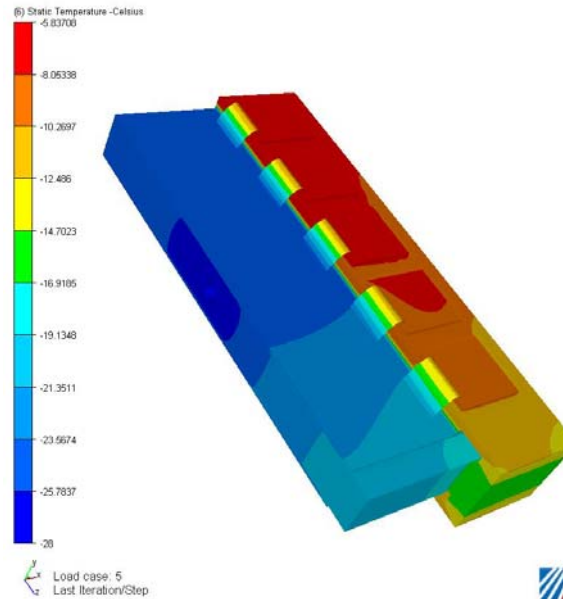

Figure 24 ¼-scale model of bridged-hybrid concept as described in the text.

Changing the bridge foam core to 10W/mK in this stagnant air model, while leaving the tube foam at 45 W/mK and sandwich foam at 3 W/mK, results in a higher peak chip temperature and increased detector surface temperature. Increased chip temperature is of lesser concern than a rise in detector temperature, because of thermal runaway considerations. For this property change, detector peak surface temperature beneath the bridge increased by 2.2ºC to -17.8ºC, with a low of -23.3 ºC at the outer edge. Correspondingly, the chip peak temperature reached a positive 2.4ºC and the bridge thermal gradient decreased to 5.0ºC.

The question may be raised as to the extent that heat passes through the air gap and the wire bonds. To this end we simulated each possibility, i.e. with and without an air gap and wire bonds. We illustrate the effects by listing the peak chip and detector temperature and the gradient in the conductive bridge material. An increase in bridge gradient signifies increased heat flow, i.e. heat normally flowing through the air gap or wire-bonds is forced through the bridge. The results of these various simulations are listed in Table 8. One will notice that the peak chip temperature without means of heat rejection through means other than the bridge is 4.53ºC, whereas when coupling is provided by the air gap and wire bonds the temperature drops to -5.84ºC. Further inspection would suggest most of this reduction comes from the presence of the wire bonds (item b versus item d). However, the difference between these two separate

effects is not altogether different. In comparing the difference in gradient through the bridge for items b-item d versus item c- item d, we see only 1.6ºC versus 1.2ºC.

Description	Chip Peak Temperature (ºC)	Bridge Gradient (ºC)	Sensor Max/Min (ºC)
a. No air, no wire bonds	4.53	10.2	-17.7/-26.5
b. No air, with wire bonds	-2.12	7.81	-19.2/-25.7
c. No wire bonds, with air	-1.52	8.2	-15.6/-25.4
d. With air, with wire bonds	-5.84	6.58	-20.0/-24.4

Table 8: Thermal results for ¼ model with and without air and wire bonds.

Our ultimate goal in modeling the bridge was to simulate a complete air enclosure around the entire model, and to use a computational fluid dynamics (CFD) code to solve a coupled heat transfer and convection problem. To achieve this goal a different approach was required for the wire bonds. In the ¼ model the wire bonds were simulated as a wide very thin sheet, which creates a meshing problem in larger models. Using the same volume for the wire bonds, we chose a narrower, thicker solid. Figure 25 depicts this wire bond geometry on a full bridge model, with chips back to back on the hybrid. The ¼ model used symmetry to reduce this larger model.

The thermal input properties for the solution shown in Figure 25 are the same as used in the ¼ model. We see that the results compare quite well for the new wire bond configuration, a peak chip temperature of -6.28ºC versus -5.83ºC.
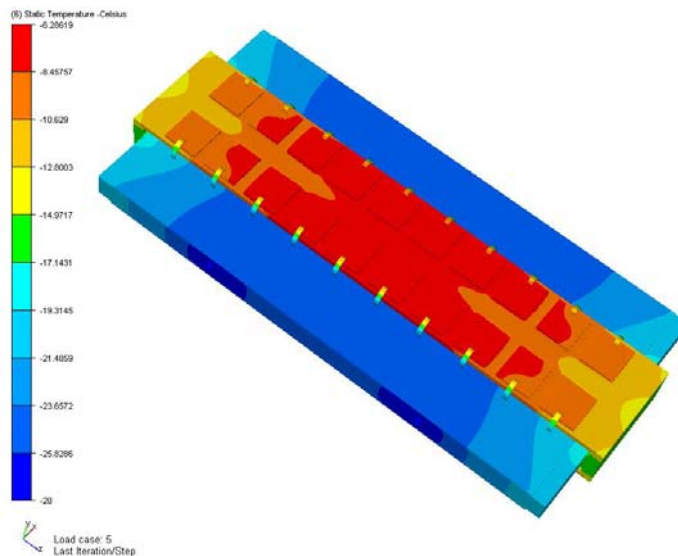

Figure 25 Full bridge model of the bridged-hybrid concept.

A CFD simulation of 3D flow effects was obtained by prescribing a very low air velocity at -15ºC (warmer than the detector) at the entrance to the surrounding air cavity – see Figure 26.

The peak chip temperature actually decreased from -6.28ºC to -7.05ºC, which was a bit surprising; no material properties were changed, except the air conductivity is now dependent upon temperature.
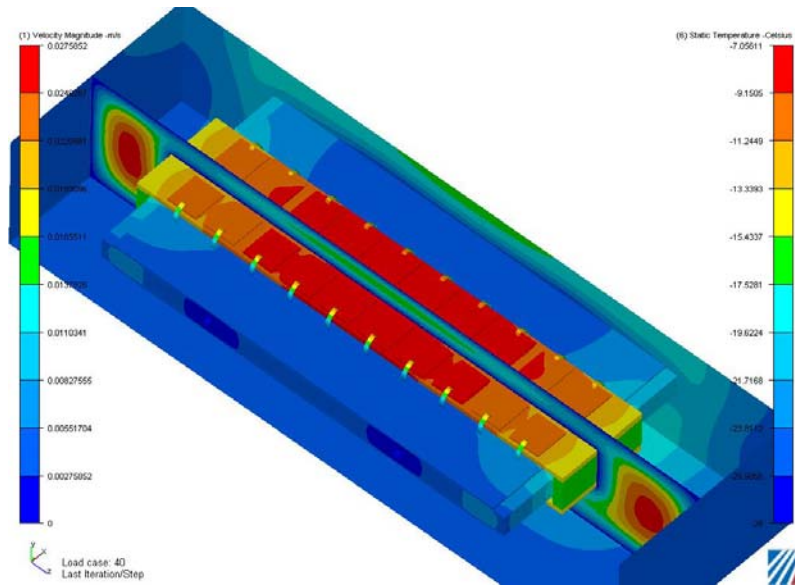

Figure 26: CFD solution of the full bridge model. The lack of complete temperature symmetry about the cutting plane in the Z direction is evident.

For increased entrance air velocity, the ability of this model arrangement to properly account for the re-distribution of heat along Z became problematic. So we changed the planes of symmetry making a model of two 10cm by 10cm detector modules in Z, with the parting plane along the stave Z axis of symmetry. We also added a short entrance section to the air box beyond the end of the solid model to smooth out the incoming air velocity (set at 0.01m/s). A solution with this improved model (entering air -15ºC) is shown in Figure 27, where two iso-plots are shown, one of velocity and one for temperature. Here the peak chip temperature is -6.18ºC and the detector surface ranges from -19.9 ºC to -25.7ºC, with an average of -23.7ºC. It would appear that heat exchange from low velocity air, warm with respect to the cold detector surface (air 10ºC above detector) does not impact the resultant detector temperature. In this solution the sandwich foam core was 3W/mK and the bridge foam and the tube support foam were both 45W/mK.
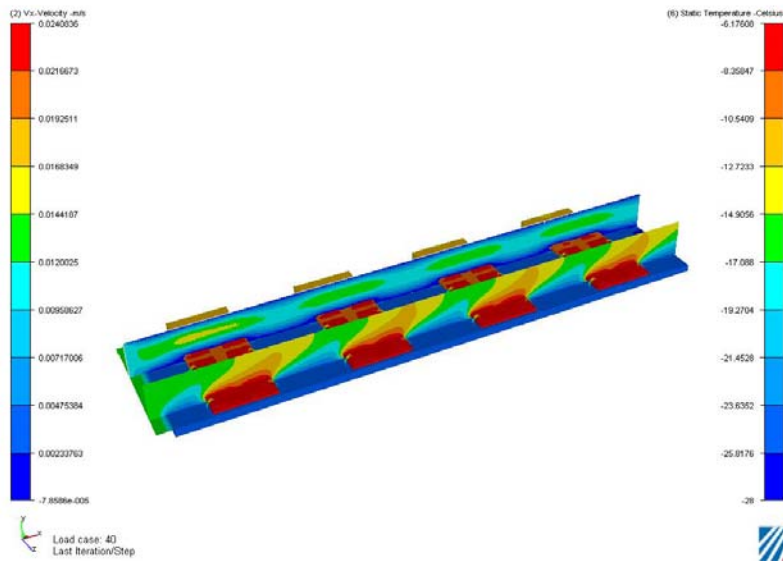
Figure 27 Multi-hybrid model of the bridged-hybrid concept. Velocity iso-plot appears in upper section (left scale) and the temperature iso-plot is lower section(right scale).

For the thermal solution depicted in Figure 28 two parameters were changed, (a) the sandwich foam core was changed from 3W/mK to 1W/mK, and (b) 1W per detector surface heating was added to each detector. The conditions of low air flow, 0.01m/s, at -15ºC remained the same. The net effect was for peak chip and detector surface temperatures to increase to -5.74ºC and -19.4ºC respectively.
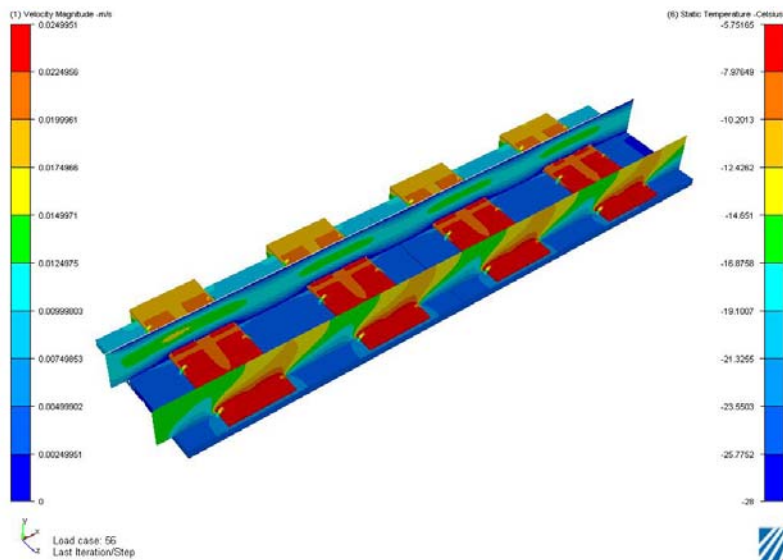

Figure 28 Example of model output with 0.01m/s air flow at -15ºC with 1W/detector surface heating. Static temperature is shown on the right and air flow velocities on the left.

Table 9 summarizes the various bridge-model results. We found that reducing the sandwich foam core from 3W/mK to 1W/mK did not have a strong effect on the detector surface temperature. The most pronounced influence on the detector surface temperature came from reducing the bridge foam core from 45W/mK to 10W/mK. Gas flow (air) across the detector surface at -15ºC and low velocity did not produce a significant effect, most likely because the convective gradient ended up being small (-20ºC to -15ºC). Additional flow conditions (temperature and velocity) remain to be studied.

Model	IC Peak Temp(C)	Bridge Gradient(C)	Sensor T_{max}(C)
¼ bridge model(baseline foam conductivity)	-5.8	6.6	-20
¼ bridge model (bridge foam reduced to 10W/mK)	+2.4	5.0	-17.8
Multi-Hybrid bridge model (baseline foam conductivity) With 0.01m/s air flow @ -15ºC	-6.2	n/a	-19.9
Multi-Hybrid bridge model (sandwich foam 1W/mK) With 0.01m/s air flow @ -15ºC, 1W per Detector	-5.74	n/a	-19.4

Table 9 Summary of different bridge model results as described in the text. Unless noted, properties are those given in Table 7.

We note the baseline design for the same conditions (0.25 W/chip, -28ºC inner tube wall temperature and no detector self-heating) yields a maximum sensor temperature of about -22ºC. The bridge-hybrid concept, as modeled above, yields higher sensor peak temperatures. However, some optimization of the design, by moving the cooling tubes outwards to reduce the thermal path length from the foot of the bridge to the cooling tube, may be possible and might result in lower peak temperatures. This possibility remains to be studied.

4.7 Long-strip Thermal Performance

The long-strip-detector modules are expected to have only one hybrid per 10 cm detector length. We have approximately modelled this as shown in Figure 29. The heat load is significantly lower than for the short-strip stave. For example, with no detector heating, 0.3 W/chip and a wall (simple U-tube) temperature of -28ºC, the hottest point on the silicon detector in the model shown in Figure 29 is about -24ºC. We have not done thermal runaway or other calculations for the long-strip staves, but anticipate that the thermal performance of the baseline design would be adequate even for C_3F_8 coolant with T_{min} = -25ºC. For a 2m long stave, the total heat load would be ½ or less (also less detector heating) than a 1 m short-strip stave assuming the same power per chip.
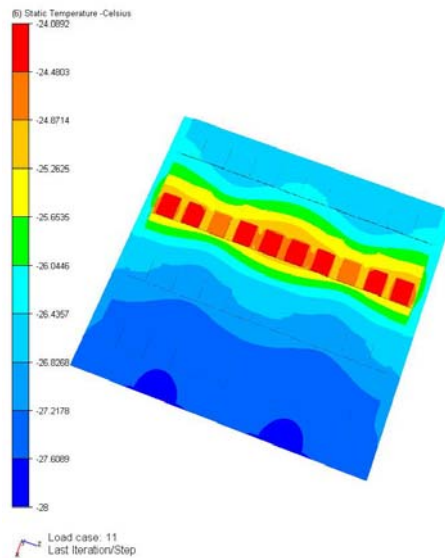
Figure 29 Model of long-strip stave section.

4.8 Thermal Runaway Estimates

The "headroom" for thermal runaway may be crudely estimated as described here. For a given set of heating parameters, we estimate the approximate wall temperature at thermal runaway and calculate the headroom from a minimum assumed coolant temperature, taking into account the ΔT values from the film coefficient and pressure drop from Table 4 (rounding to the nearest $^\circ$C, given the uncertainties in these estimates).

Heating	Tube	Runaway T	T_{min}	T_{film}	T_P	Headroom	T_{min}	T_{film}	T_P	Headroom
			C3F8				**CO2**			
0.3 W, 1 mW	Single	-14	-25	4	1	6	-35	3	1	17
0.3 W, 2 mW	Single	-21	-25	4	1	-1	-35	3	1	10
0.125 W, 1 mW	Single	-10	-25	4	1	10	-35	3	1	21
0.50W, 1 mW	Single	-20	-25	4	1	0	-35	3	1	11
0.3 W, 1 mW	Triple	-2	-25	3	2	18				
0.5 W, 2 mW	Triple	-10	-25	3	2	10				
0.3 W, 1 mW	Single Foam	-5	-25	4	1	15				

Table 10 Rough estimate of headroom in $^\circ$C for thermal runaway calculated as described in the text for single U-tube and triple U-tube(with honeycomb core) and for a single U-tube with conducting foam replacing the honeycomb core for different heating conditions and fluids.

We do this separately for very cold conditions (T_{min} = -35°C assumed to be applicable to CO_2) and current conditions (T_{min} = -25°C assumed applicable to C_3F_8 with current pressure regulation and other conditions). The results are given in Table 10 for the different values of chip power and detector self-heating (in mW/mm^2) at 0°C for the nominal concept in which detectors with hybrids are glued directly to the bus-cable.

A somewhat more detailed calculation has been performed for CO_2. The heat transfer (film) coefficient is held fixed (at 6833 W/m^{2}K as calculated at the entrance to the stave for a quality factor of 0.05) for a bulk fluid temperature of -34°C. The ¼ scale FE model of the

nominal design is run with these assumptions varying the detector self-heating for two values of chip power. The results are shown in Figure 30. We have also estimated the effect of increased total power on the heat transfer coefficient assuming fixed mass flow. The boiling film coefficient increases and the convective film coefficient remains the same for increased power. For example, we estimate that the film temperature drop at the entrance would change from about $2.5^{o}C$ (240 W) to about $3.9^{o}C$ (500 W). Thus, assuming a fixed film heat transfer coefficient is not an unreasonable approximation to estimate the headroom against thermal runaway but a more exact calculation would take into account the temperature dependence of the coefficient as thermal runaway is approached.
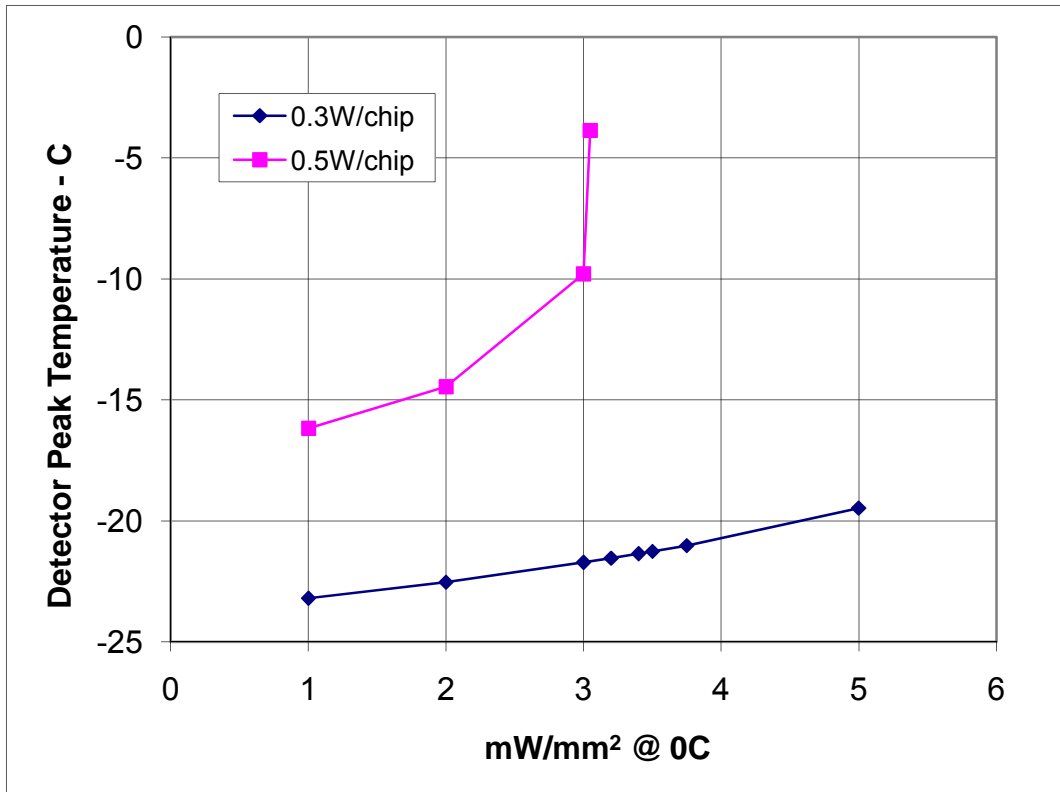

Figure 30 Detector peak temperature vs. detector self-heating for two values of the power per chip for CO_2 fluid conditions described in the text for the nominal stave design.

Similar estimates have been made for C_3F_8 for T_{min} about $-25^{o}C$. The results are shown in Figure 31. The peak detector temperature is estimated from a ¼-scale model for different stave configurations (single U-tube with honeycomb core, single U-tube with foam core with K=15 W/mK and triple-U-tube with honeycomb core) for the values of the heat transfer coefficient (h) given in Figure 31. The lower values of h (1436 and 1206) are calculated from the fluid parameters(at $-24^{o}C$) and a heat load corresponding to 0.3W/chip for the different stave tube configurations near the entrance to the stave assuming a quality factor of 0.05. The results for h = 3000 W/m^2K are shown for comparison in two cases. We note that the value of h depends on the heat flux, rising as the heat flux increases. A more exact calculation would include this dependence. Thus, for the example of the single U-tube with conducting foam, the actual

response curve would lie between the curve calculated for a fixed h of 1436 and the curve calculated for h = 3000. We note a value of h ~ 3000 is calculated for a heat load (single U-tube) of about 500 W, or roughly at thermal runaway.
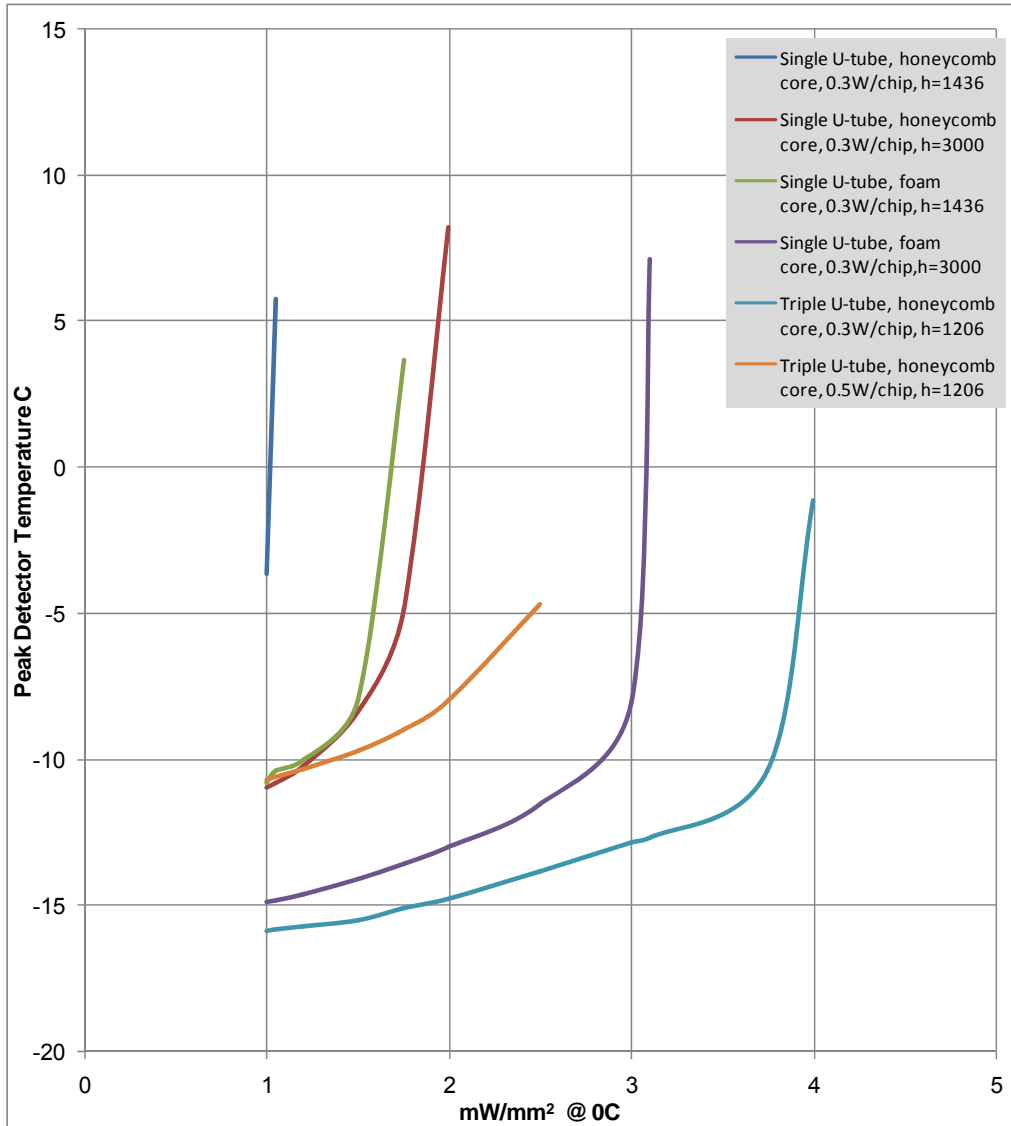

Figure 31 Peak detector temperature vs detector self-heating for different stave configurations and heat transfer coefficients, estimated as described in the text.

Thermal runaway estimates have also been made for the bridged-hybrid design for CO_2 coolant, again assuming a bulk fluid temperature of -34°C (entrance), a film coefficient of 6833 W/m²K and 0.3 W/chip. The results are shown in Figure 32 for two different values of the thermal conductivity of the bridge foam in the stave (the core foam is 3 W/mK). It may be possible to reduce T_{max} by moving the cooling tubes towards the foot of the bridge but this option has not been studied. In addition, the increasing the core foam conductivity would also increase the headroom.
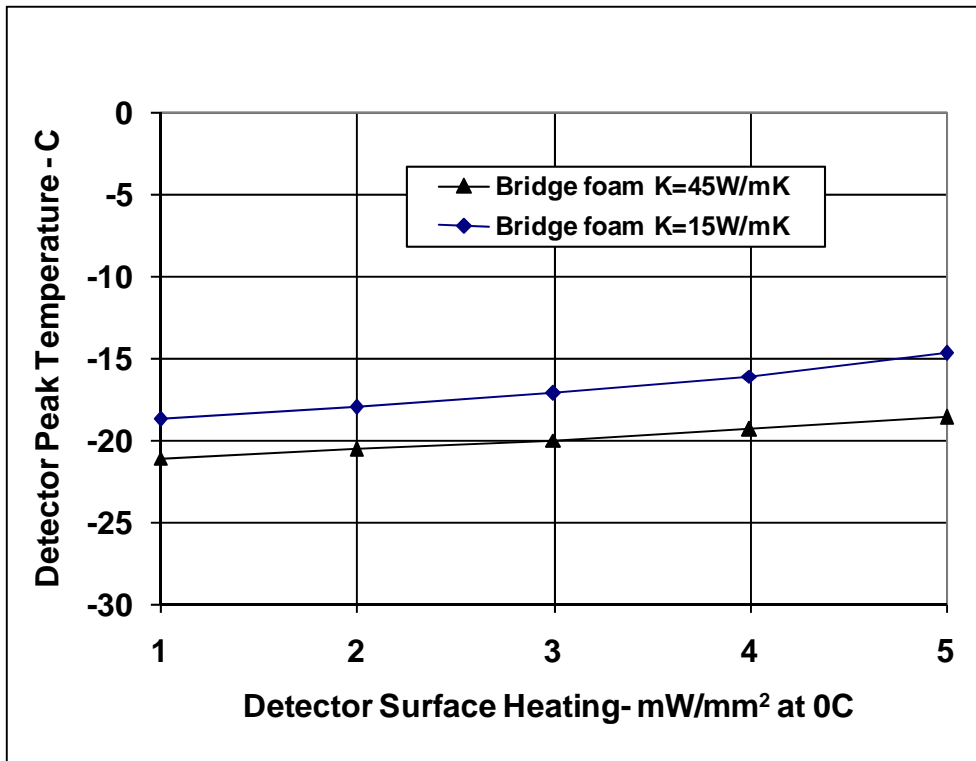
Figure 32 Detector peak temperature for a bridged-hybrid design for two different values of the carbon foam conducting heat from the foot of the bridge to the cooling tube structure. Estimated for 0.3 W/chip and a film coefficient of 6833 W/m²K.

We conclude the following from the studies of thermal runaway:

- The baseline design with a honeycomb core and a simple U-tube does not have acceptable headroom for T_{min} = -25°C, representative of current cooling expectations with C_3F_8

- The baseline design with a triple U-tube and a honeycomb core has acceptable headroom for T_{min} = -25°C, representative of current cooling expectations with C_3F_8

- The baseline design has acceptable headroom for a single U-tube and honeycomb core for $T_{min} \sim$ -35°C, which could be applicable to CO_2 or perhaps mixtures of C_3F_8 with other fluorocarbons.

- A modified design with thermally conducting carbon foam instead of honeycomb and a single U-tube may have acceptable headroom for C_3F_8 with T_{min} = -25°C

- The headroom could be increased by small amounts from optimization of the carbon-fiber facings (gain $\sim$ 1°C) and from improved thermal conductivity of the bus-cable (gain $\sim$ 1- 3°C). These possible gains would be most important to realize if C_3F_8 with T_{min} about -25°C were used.

- A bridged-hybrid concept has sufficient headroom for for T_{min} ~ -35°C, and some further optimization of the basic design (placement of cooling tubes) may be possible.

5. Mechanical Performance

We describe in this section calculations done on some of the basic mechanical properties of a stave. We first present concepts for the support of the barrel stave. We then summarize measurements and calculations of the gravitational deflection of a stave. Initial estimates using FE models for the distortions of a stave upon cooling from assembly at room temperature to the operating temperature are given. Calculations related to the shear stress at the adhesive joint between dissimilar materials i.e. at the outer tube wall interface are described.

5.1 Stave Support Concepts

We have looked briefly at two options for supporting the staves in the barrel region and the impact on some elements of the stave design. One option is to support the staves solely at the ends (for a 1 m length). This option is illustrated conceptually in Figure 33 (left). In this case it is desirable to limit the stave radial deflection to less than 50-100 microns such that the uncertainty in this deflection does not substantially affect the resolution through coupling of the radial uncertainty into a ϕ uncertainty in which the resolution is about 80 $\mu/\sqrt{12}$. A consequence of this assumption is to increase the stiffness requirement of the stave. Practically this means increasing the thickness of the facings since the overall thickness of the stave is largely fixed by the size of the cooling tube. The second option is to support the staves from a shell-like structure. This concept is illustrated in Figure 33 (right) for the case in which two layers of staves are supported by a single shell. In this case, the thickness of the facings of the staves can be significantly less, since the staves are supported more frequently. In addition, the initial installation of the staves is easier for a shell-like support.
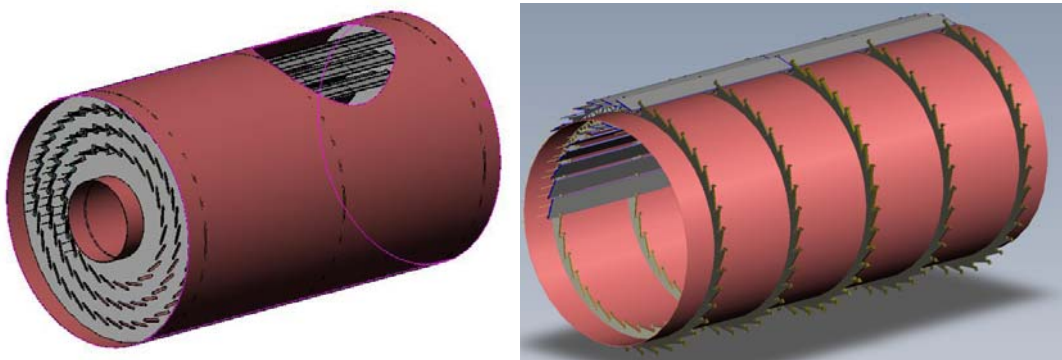
Figure 33 (Left) Concept for supporting staves at 1 m intervals. A 2 m-long barrel is shown, including an external shell to support the three endplates locating the staves. (Right) Concept for supporting staves from a thin shell. Lightweight rings are spaced (about every 0.5 m in this figure) to which the staves are attached at the sides both on the outside and inside of the shell.

A detailed design of the support (for either option) is beyond the scope of our study. Our preference for further work is to develop the shell support option. We note that the stave can be made stiff enough with a limited number of support points (e.g. every 50 cm) on a shell such

that a survey of module positions on a stave relative to the attachment points can likely serve as an initial input to alignment with tracks.

We also note that tilt angle, the angle of the normal to the stave relative to a radial vector through the center of the stave, depends on the thickness of the stave, which in turn depends on the choice of cooling tube diameter (coolant) and to a lesser extent on the stiffness desired (the facing thickness). The thinnest possible stave is likely to be desirable (and also to minimize the radiation length) to better match the Lorentz angle expected for the chosen silicon detectors for the SLHC upgrade.

5.2 Stave Deflections

A simple measurement of the mid-point deflection of the 1 m prototype (#3) was performed. The prototype was simply supported with a span of 40 inches (1.016 m) and a load of up to 0.96 lbs applied at the center. The measured deflection at this weight was 0.31 mm. This prototype used honeycomb core bonded to the facings with a rigid, room temperature cured adhesive.

Core shear is essential to achieving bending of the laminate facings about the sandwich neutral axis whether it is a foam or honeycomb material. The deflection of a sandwich is composed of a bending component, i.e., facings about their neutral axis and deflection due to core shear. Insufficient core stiffness results in shear deformation and increased deflection. Core shear stiffness will come from two contributions; (a) the adhesively bonded honeycomb core pieces that straddle the U-tube (cooling) and the cooling tube, which also is bonded to the facings. The same applies if carbon foam replaces the honeycomb. Our studies of this sandwich make-up suggest that the shear resistance of the tube, assuming good bonding, plays a distinct contributing role.

In preparation for this prototype static load test, tensile tests were performed on the K13D2U laminate used for the prototype construction. The 10-layer prototype laminate had a fiber orientation of 90/0/0/0/0/s, with a measured thickness of 0.684mm. An average of three tensile specimens yielded a tensile modulus of 379.2GPa and Poisson's ratio of 0.015. We had based our laminate micromechanics predictions on an assumed thickness of 0.704mm (quite close to actual) and 55% fiber fraction. The predicted laminate properties for 55% fiber fraction are 397GPa tensile modulus and a Poisson' ratio of 0.015; predicted tensile modulus matched within 4.5% of measurements.

An FEA model was made of the prototype sandwich construction. This model was used to predict the deflection under an input load condition that simulated a four point bend test. The deflection at the quarter points from this solution was used to extract the *effective* shear modulus for the core and cooling tube. The result of this prediction was a core shear modulus of 128MPa. Next in this process was to conduct an actual four point bend test using the short prototype #2.

The bend test of prototype #2 yielded a central deflection of 0.118mm for 26.59N loads at the quarter points. A predicted central deflection prediction using a shear modulus of 128MPa agreed with this test within 15%; our prediction was lower. This analytic solution used the laminate tensile modulus test data (379GPa).

The core shear modulus implied by the four bend test was lower than published by the supplier for honeycomb, as one would expect. Reduction in shear modulus is caused by several factors, (a) adhesives used in joining, albeit a rigid adhesive and (b) the presence of the bonded cooling tube, which takes up space normally filled with honeycomb. The adhesive contribution

for the honeycomb and cooling tube (compliant CGL7918) would contribute to our under prediction of the central deflection since the FEA assumed zero compliance at the bonded interfaces.

Returning to the 1 m prototype test, an analytical solution based on our predicted 128MPa shear modulus coupled with the micromechanics generated laminate properties was 12% higher than the 0.31mm measured value.

5.3 Stave Distortions

FEA thermal strain simulations were made for a stave 7 cm wide with alternating detector modules, front to back. This arrangement accentuates unbalanced thermal strains across the sandwich, largely resisted by the sandwich bending stiffness. In anticipation of this thermal strain and gravity sag issues, we configured a stave with a 10-layer, 0.7mm thick, high axial modulus K13D2U facing. One of the simulations is shown in Figure 34, where the out-of-plane thermal strain is 11microns.

This differs from the current concept of a 10cm wide stave that has to a very large extent complete thermal symmetry front to back. Thermal symmetry played a role, as did lower radiation length, in choosing to reduce the composite sandwich facing from 0.7mm to 0.21mm. With a well balanced thermal design, a very stiff composite facing becomes less important. However, the final factor to be considered in the sizing the facing thickness is whether the stave is supported at its end (1m unsupported length) or every 50cm as in the support shell concept. More work is needed to resolve this aspect; however, the thermal strain would appear at this stage not to be an issue.
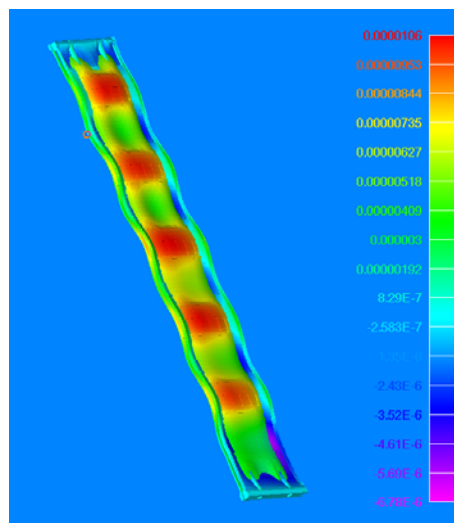
Figure 34 FEA thermal solution for 50ºC cool-down from room temperature to -25ºC. Out-of-plane distortions are ~11microns for a 7cm wide stave with alternating front to back detector modules.

We also assessed the module deflection due to internal pressure on the aluminum cooling tube with this model. Outward distortion was less than a micron for 8bar internal cooling tube pressure. We note that the tube wall thickness would have to be adjusted to meet higher pressure requirements for different coolants and assumed fault conditions. Fixing the tube wall based on

fault conditions e.g. 15 bar for C_3F_8 and 100 bar for CO_2 would likely result in negligible tube distortions under normal operating conditions.

5.4 Shear Stress and Other Items

The issue of shear stress between the aluminum coolant pipe and the surrounding foam has been addressed by calculation. For the purpose of this discussion we wish to solely address this joint, however, we also consider our remarks applicable to joining the cooling tube directly to composite facings.

To examine the magnitude of the shear stress in the bonded joint we draw upon work reported by W.T. Chen and C.W. Nelson in "Thermal Stresses in Bonded Joints".[9] The results of their work provide good approximations as long as the elastic modulus of the materials are at least 10 times the adhesive modulus and the thickness of joined materials are 10 times the adhesive thickness.

As Chen points out, the shear stress at the center of the joint is zero and gradually increases to a maximum at the free edge. For two elastic materials, joined by a single adhesive layer he gives the approximation for the maximum shear stress for a ΔT as:

$$\lambda = \frac{(\alpha_1 - \alpha_2)\Delta T G}{\beta t}, \text{ where } \beta = \sqrt{\frac{G}{t}\left(\frac{1}{E_1 t_1} + \frac{1}{E_2 t_2}\right)}.$$ The expansion coefficients are α

for the joined materials. Young's moduli for the two materials are E1 and E2 respectively. The adhesive shear modulus is G and bond-line thickness t. The thicknesses of the joined bodies are t_1 and t_2.

Unfortunately, the knowledge of the material properties necessary to determine the shear stress is limited. To date we have used EG7658, a semi-rigid conductive epoxy, and a very compliant adhesive, CGL7018, for joining materials that differ significantly in CTE. The EG7658 is an AlN-filled flexible epoxy adhesive and the CGL7018(also AlN-filled) is more a "gel-like" conductive adhesive. EG7658 is significantly more rigid at room temperature. CGL7018 can not sustain stress due to its plastic nature; it has less than 0.7kPa shear strength at room temperature. However, EG7658 has lap-shear strength of ~7MPa at room temperature. Thus, we are more concerned when more rigid materials like EG7658 are used, particularly whether the shear stress will break the adhesive joint.

Lacking a shear modulus for EG768, we use AI Technology's value for ME7159, another thermally conductive flexible adhesive. Using this property and based on the expressions developed by Chen, et al, we estimate a 1.6 MPa maximum shear stress using a 100 micron thickness of semi-rigid material like EG7658. This is significantly lower than the published strength for EG7658 (7MPa). We conclude that shear stress is not a large problem for the 60ºC differential that this calculation was based on. We have already noted that no degradation in thermal performance was observed for the prototypes after cycling from room temperature to -35ºC. However, the region of significant shear stress occurs only in the last few millimeters of the structure and thus the effects would be difficult to observe. We also note that the maximum shear stress is independent of the length (e.g. from 0.3-2m) for a reasonable range of material properties used. Careful attention to this issue would be required during the future design and prototype phase.

6. Stave Material Estimates

The radiation lengths of a few options for the construction of the stave are presented in this section. The radiation length estimates do not include the following: bus-cable(and adhesive gluing it to the stave), coolant present in the coolant tubes, additional material for fasteners (to supporting shells or plates), strain relief (for services), modules or end-of stave cards. The radiation length is estimated by averaging over a length of 1 m and a width of 0.108 m. The radiation lengths are estimated by extrapolation from the measured weights of the prototypes (section 2.4) and by direct calculation.

A range of radiation lengths is given in Table 11 for different configurations of the stave. The range reflects uncertainties in the tube type (aluminum, stainless steel) facing thickness and density, type and amount of thermal and other adhesives used and the overall thickness of the stave. The four cases shown arise from the studies of thermal runaway and represent stave configurations that would meet thermal runaway requirements. The first item in Table 11 would be applicable to CO_2 cooling for the baseline stave design with modules glued directly to the bus-cable. The second and third cases would be applicable to C_3F_8 cooling for T_{min} = -25°C. The fourth case would be representative of CO_2 cooling in the case the bridged-hybrid concept were used.

Description	Al Tube X_0 (%)	SS Tube X_0 (%)
Single Al U-tube (3mm OD, 2.2mm ID), honeycomb core	0.35-0.40	0.45-0.50
Single Al U-tube (6mm OD, 5.3mm ID), foam core (ρ = 0.2 g/cc)	0.65-0.7	0.85-0.9
Triple Al U-tube (>6mm OD, >5.3mm ID), honeycomb core	0.65-0.7	0.85-0.9
Single Al U-tube (3mm OD, 2.2 mm ID), foam core (ρ = 0.2 g/cc)	0.40-0.45	0.50-0.55

Table 11 Radiation length X_0 (%) for different stave configurations as described in the text.

An example of the radiation length calculation is shown in Table 12. The conditions for this particular example are:

- For CO_2: single aluminum U-tube (3mm OD, 2.2mm ID), honeycomb core of thickness 0.495 cm (same as prototype), AlN-filled thermal adhesive
- For C_3F_8: single aluminum U-tube (6mm OD, 5.3mm ID), thermally conducting foam core (ρ = 0.2 g/cc), 0.6 cm thick, AlN-filled thermal adhesive.

	CO2				C3F8			
	Weight	Density	X0		Weight	Density	X0	
	grams	g/cc	(g/cm^2)	X0(%)	grams	g/cc	(g/cm^2)	X0(%)
Facings	74	1.7	57	0.12	74	1.7	57	0.12
Honeycomb	12	1.7	57	0.02	15	1.7	57	0.02
Core foam	0	0.2	43	0.00	118	0.2	43	0.25
Tube (bare)	18		24	0.07	34		24	0.13
Tube foam	38	0.55	43	0.08	0	0.55	43	0.00
Thermal adhesive	18		30	0.06	34		30	0.10
Epoxy	24		42	0.05	28		42	0.06
Total	185			0.40	303			0.70

Table 12 Example of a radiation length estimate as described in the text.

7. Conclusions

A principal conclusion of these studies is that the design of the mechanical/cooling aspects of the baseline (modules glued directly to bus-cable on stave) integrated stave concept (for short strip detectors) depends critically on the assumed coolant temperature. A minimum CO_2 coolant temperature of about -35^oC would result in an integrated stave with substantial headroom against thermal runaway (assuming electronics and heating parameters about those considered here) and a radiation length (of the mechanical/cooling core element only) of 0.30-0.35% X_0. Alternatively, if C_3F_8 coolant as currently implemented, with a T_{min} of about -25^oC, were selected, then it would be possible to construct a stave to meet thermal requirements, but with increased radiation length, in the range 0.45-0.7% X_0. The thermal performance requirements for long-strip detector staves are less demanding. For a given coolant, the mechanical properties of the stave, in particular the stiffness and stability (vibrational modes) would have to be adjusted to meet requirements in a combined design with the overall supporting structure. A significant prototype program to validate the thermal performance (for a given coolant) and to measure distortions and deflections would be required in addition to a detailed design effort.

Acknowledgments

We gratefully acknowledge the excellent support of the members of the machine shop and plating/cleaning shop of the Lawrence Berkeley National Laboratory.

References

[1] Layout Requirements and Options for a New Inner Tracker for the ATLAS Upgrade, N.P. Hessey and J. Tseng, ATL-P-EP-0001 Rev. G, 11 June 2007 and subsequent updates.

[2] We note that an integrated stave design was proposed for the CDF Run IIb upgrade – see T. Akimoto et al, The CDF Run IIb Silicon Detector: Design, preproduction, and performance, Nucl.Instrum.Meth., A 556 (2006) 459.

[3] P. B. Whalley Boiling Condensation and Gas-Liquid Flow", Oxford Science Publications (1987).
http://journals.cambridge.org/action/displayAbstract?fromPage=online&aid=394462

[4] J. C. Chen, " A correlation for boiling heat transfer to saturated fluids in convective flow", ASME Paper 63-HT-34

[5] Frank Krieth and Mark S. Bohn, "Principles of Heat Transfer" 5th Edition, PWS Publishing Company.

[6] The calculations are at http://www-physics.lbl.gov/~gilg/ATLASUpgradeRandD/StaveReview/StaveNoteReferences/

[7] The parameterization is from N. Unno, private communication. A temperature dependence of the current $\frac{I(T)}{I(T_0)} = \left(\frac{T}{T_0}\right)^2 \exp\left(-\frac{E_g}{2k_B}\left(\frac{1}{T} - \frac{1}{T_0}\right)\right)$, where E_g=1.23 eV, k_B=8.62x10^{-5} eV/K is assumed. A sensor thickness of 320 microns and a bias voltage of 600 V are assumed.

[8] Low-density, carbon foams are under active development for use in SLHC pixel detector local supports. Foam with density 0.09-0.25 is available from multiple sources and with nominal K values in the range 5-30, depending on the source and the density.

[9] W. T. Chen and C. W. Nelson, "Thermal stresses in bonded joints," IBM. J. Res. Develop., vol. 23, no. 2, pp. 179–187, 1979.
http://www.research.ibm.com/journal/rd/232/ibmrd2302I.pdf